

Research Paper

Dual-targeted magnetic mesoporous silica nanoparticles reduce brain amyloid- β burden via depolymerization and intestinal metabolism

Ni Liu^{1,2}, Xiaohan Liang^{1,2}, Changwen Yang^{1,2}, Shun Hu^{1,2}, Qingming Luo^{1,2,3}, Haiming Luo^{1,2} ✉

1. Britton Chance Center for Biomedical Photonics, Wuhan National Laboratory for Optoelectronics, Huazhong University of Science and Technology, Wuhan, China.
2. MoE Key Laboratory for Biomedical Photonics, School of Engineering Sciences, Huazhong University of Science and Technology, Wuhan, China.
3. School of Biomedical Engineering, Hainan University, Haikou, Hainan 570228, China.

✉ Corresponding author: Haiming Luo, hemluo@hust.edu.cn; Britton Chance Center for Biomedical Photonics, Wuhan National Laboratory for Optoelectronics–Huazhong University of Science and Technology, 430074, Wuhan, Hubei, China. Fax: +86-27-87792034; Tel: +86-27-87792033.

© The author(s). This is an open access article distributed under the terms of the Creative Commons Attribution License (<https://creativecommons.org/licenses/by/4.0/>). See <http://ivyspring.com/terms> for full terms and conditions.

Received: 2022.06.27; Accepted: 2022.09.03; Published: 2022.09.11

Abstract

Rationale: Active removal of excess peripheral amyloid- β ($A\beta$) can potentially treat Alzheimer's disease (AD). However, the peripheral clearance of $A\beta$ using an anti- $A\beta$ monoclonal antibody (mAb) cannot remove PET-detectable $A\beta$ within the brain. This may be due to the inability of mAb to cross the blood-brain barrier (BBB) to degrade insoluble brain $A\beta$ plaques and block liver dysfunction.

Methods: We developed a dual-targeted magnetic mesoporous silica nanoparticle (HA-MMSN-IF12) through surface-coupled $A\beta_{42}$ -targeting antibody IF12 and CD44-targeting ligand hyaluronic acid (HA).

Results: HA-MMSN-IF12 had a high binding affinity toward $A\beta_{42}$ oligomers ($K_d = 1.27 \pm 0.34$ nM) and revealed robust degradation of $A\beta_{42}$ aggregates. After intravenous administration of HA-MMSN-IF12 into ten-month-old APP/PS1 mice for three weeks (4 mg/kg/week), HA-MMSN-IF12 could cross the BBB and depolymerize brain $A\beta$ plaques into soluble $A\beta$ species. In addition, it also avoided hepatic uptake and excreted captured $A\beta$ species through intestinal metabolism, thereby reducing brain $A\beta$ load and neuroinflammation and improving memory deficits of APP/PS1 mice. Furthermore, the biochemical analysis showed that HA-MMSN-IF12 did not detect any toxic side effects on the liver and kidney. Thus, the efficacy of HA-MMSN-IF12 is associated with the targeted degradation of insoluble brain $A\beta$ plaques, avoidance of non-specific hepatic uptake, and excretion of peripheral $A\beta$ through intestinal metabolism.

Conclusions: The study provides a new avenue for treating brain diseases by excreting disease-causing biohazards using intestinal metabolism.

Key words: Alzheimer's disease, amyloid- β ($A\beta$), magnetic mesoporous silica nanoparticles, $A\beta$ clearance, $A\beta_{42}$ -targeting antibody.

Introduction

Alzheimer's disease (AD), a progressive and destructive disorder, is characterized by abnormal amyloid- β ($A\beta$) protein deposits in the brain [1]. These neurotoxic $A\beta$ peptides form insoluble filaments that accumulate into amyloid plaques in the brain and blood vessels. Abnormal $A\beta$ accumulation precedes neurodegeneration and cognitive decline in familial and sporadic AD, indicating that abnormal $A\beta$ brain metabolism has a central role in AD pathogenesis.

Pathological $A\beta$ deposition could be due to an altered balance between overproduction and elimination. Evidence indicates that active removal of excess peripheral $A\beta$ could be a potential treatment strategy for AD [2]. Immunotherapy with anti- $A\beta$ antibodies is the most likely treatment strategy for disease management. Various peripheral interventions have been attempted, including $A\beta$ vaccination, intravenous anti- $A\beta$ antibody administration, and

intravenous immunoglobulin administration, to slow down A β deposition and reduce AD. However, peripheral clearance of A β with the anti-A β monoclonal antibody (mAb) solanezumab in clinical studies cannot appear to remove PET-detectable A β from the brain, so alterations in peripheral A β metabolism may not be associated with AD [3]. Many factors may cause the failure of solanezumab to remove A β deposits from the brain. However, the most likely reason is that once A β is sequestered in insoluble plaques, a simple concentration gradient might not dissolve the deposits. This could be due to immune complex formation with soluble A β in the blood after intravenous infusion of anti-A β monoclonal antibodies, with a half-life of days to weeks. In contrast, the half-life of free A β peptides is several hours. Therefore, effective strategies to remove insoluble A β aggregates from the brain will be the key to reducing the brain A β burden.

A β clearance may also depend on the entry of anti-A β antibodies into the brain, but only about 0.1-0.2% of peripherally injected antibodies can enter [4]. Various strategies, including focused ultrasound [5], intranasal administration [6], or multiple formulations [7], can increase the uptake of antibodies and biomacromolecules in the brain. Receptor-mediated transcytosis is currently the most commonly used strategy for delivering antibodies to the brain. In this approach, antibodies are fused to antibodies targeting transferrin [8] or insulin receptors [9] located on the surface of BBB-forming endothelial cells. Transferrin receptor (TfR) and low-density lipoprotein receptor-related protein-1 (LRP1) enhance brain uptake of antibodies through antibody fusions [10-14] or bispecific constructs [15, 16]. However, TfR and LRP1 are widely expressed in cells of various tissue, including brain endothelial cells, hepatocytes, and tumor cells, which would increase the non-specific accumulation of TfR-modifying drugs in these tissues, especially in the liver. Furthermore, strategies for drug delivery to the brain using anti-TfR antibodies suffer from low specificity to brain tissue and immunogenicity [15, 17, 18].

Hyaluronic acid (HA) is a biodegradable, biocompatible, and non-immunogenic glycosaminoglycan that is recognized by the CD44 receptor on the surface of endothelial cells [19]. Although HA targets CD44-overexpressing tumor cells [20], it can mediate its conjugates across the BBB via endocytosis. Nanomaterials retain the properties of antibodies and offer better design flexibility and functionality to combine therapeutic agents in one structure [21]. However, anti-A β mAb-modified liposomes [22], polymeric nanoparticles [23], inorganic nanoparticles [24, 25], and biomimetic nanozymes [26] can clear

peripheral A β in AD transgenic mice. The administered nanomaterials accumulate in the liver, resulting in A β accumulation being captured by the nanomaterials. In contrast, rodent studies have shown impaired hepatic A β degradation in AD subjects [27]. The abundance of these toxic and non-degradable A β may be deposited in the liver, accelerating the pathological process of AD [28]. Therefore, overcoming liver dysfunction ensures the targeted clearance of insoluble A β in the brain and reduces its A β burden.

The accumulation of nanodrugs in the liver is regulated by their size, charge, surface modification, and their choice [29]. Mesoporous silica nanoparticles (MSNs) are relatively safe and porous, with good biocompatibility and easy surface modification. MSN particles larger than 100 nm depicted low cytotoxicity, while particles smaller than 50 nm significantly induce cell necrosis [30, 31]. Based on recent findings and our previously developed anti-A β_{42} monoclonal antibodies (mAbs) [32], we synthesized 413 nm functionalized magnetic mesoporous silica nanospheres with surface-bound anti-A β mAb 1F12 and CD44-targeted HA ligands (HA-MMSN-1F12) to evaluate its ability to depolymerize A β aggregates into monomers *in vitro*. In addition, APP/PS1 transgenic mice were used to evaluate the ability of HA-MMSN-1F12 to cross the BBB and its biodistribution and therapeutic effects. This innovative concept of using nanotechnology to solve the problem of AD liver dysfunction and the inability of mAbs to enter the brain to degrade insoluble brain A β plaques opens up a new avenue for AD treatment.

Results

Characterization of HA-MMSN-1F12 with dual targeting of A β_{42} and CD44

A dual-targeted A β clearance system based on MMSN was constructed to achieve efficient clearance of A β in the brain. The anti-A β_{42} -targeting antibody 1F12 was introduced to capture A β_{42} peptides, and the surface-coupled CD44-targeting ligand HA efficiently enhanced the brain entry of HA-MMSN-1F12 (Figure 1A). HA-MMSN-1F12 was characterized for size, shape, hydrodynamic diameter, zeta potential, and binding affinity for A β species. After surface modification, the hydrodynamic diameter of HA-MMSN-1F12 ranged from 413 to 478 nm. Moreover, the PDI value decreased from 0.049 to 0.045, supporting the improved stability of HA-MMSN-1F12 (Figure 1B-C). HA-MMSN-1F12 depicted a negative zeta potential of -13.03 ± 0.12 mV (Figure S1A). Fourier transform infrared (FT-IR) spectroscopy, SDS-PAGE, and Western blotting confirmed that 1F12

was successfully immobilized on the MMSN surface (Figure S1B-C). Furthermore, HA-MMSN-1F12 had good stability of HA-MMSN-1F12 in plasma with less adsorption to serum albumin and no specificity (Figure S3). ELISA and IP-Western blotting data revealed that HA-MMSN-1F12 retained the characteristics of 1F12 and could specifically recognize soluble $A\beta_{42}$ and $A\beta_{42}$ Arc, monomers, and oligomers, but not $A\beta_{40}$ (Figure S4A-B). The core of the MMSN consists of numerous magnetic nanoparticles generating nuclear magnetic signals via magnetic resonance imaging (MRI). As shown in Figure S2, the T2 relaxation time of the MMSN is 94.89 ms, and the saturation recovery (SR) pulse showed that the MMSN had a good T1 mapping. These results indicated that the MMSN had a good MRI signal.

In addition, the minimum detection limit of $A\beta_{42}$ Os was 0.5 pM, providing excellent sensitivity for

the detection of peripheral and central $A\beta_{42}$ (Figure S5). Indirect ELISA depicted that the K_d values of HA-MMSN-1F12 for binding to $A\beta_{42}$ were 0.77 ± 0.09 nM for $A\beta_{42}$ Ms, 1.27 ± 0.34 nM for $A\beta_{42}$ Os, 0.98 ± 0.17 nM for $A\beta_{42}$ ArcMs, and 1.27 ± 0.26 nM for $A\beta_{42}$ ArcOs, respectively, comparable to the observed 1F12 values (0.95 ± 0.01 nM, 0.82 ± 0.01 nM, 0.85 ± 0.18 nM, and 1.31 ± 0.17 nM, respectively) (Figure 1D-E). In contrast, HA-MMSN showed no affinity toward different $A\beta_{42}$ conformations (Figure 1F). Immunofluorescence imaging of brain sections from eight-month-old APP/PS1 mice revealed that ThioS-positive $A\beta$ plaques colocalized with Cy5-labeled 1F12 and HA-MMSN-1F12, but not with HA-MMSN-IgG (Figure 1G and Figure S4C), depicting the binding specificity of HA-MMSN-1F12 toward $A\beta$ plaques. Therefore, HA-MMSN-1F12 showed a preference for capturing $A\beta_{42}$ species rather than $A\beta_{40}$.

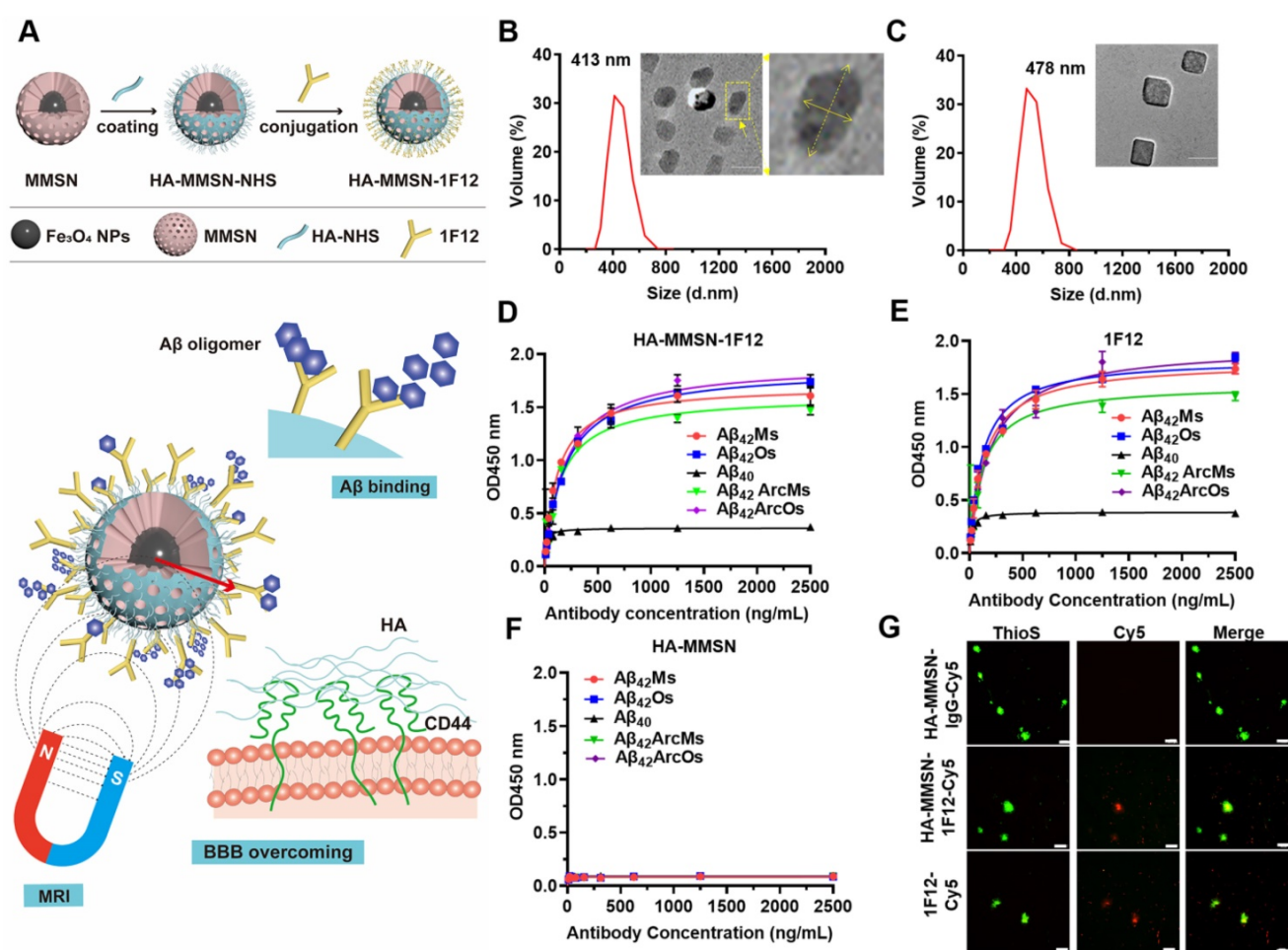


Figure 1. Synthesis and characterization of HA-MMSN-1F12. (A) Schematic diagram of HA-MMSN-1F12 synthesis. Particle size and TEM images of (B) HA-MMSN and (C) HA-MMSN-1F12, aspect ratio 2. The binding affinity of (D) HA-MMSN-1F12, (E) 1F12, and (F) HA-MMSN is based on different $A\beta$ conformations. (G) Confocal imaging of brain sections from eight-month-old APP/PS1 mice incubated with Cy5-labeled 1F12, HA-MMSN-1F12, and HA-MMSN-IgG and counterstained using ThioS. Cy5 (red), ThioS (green), and scale bar, 50 μ m.

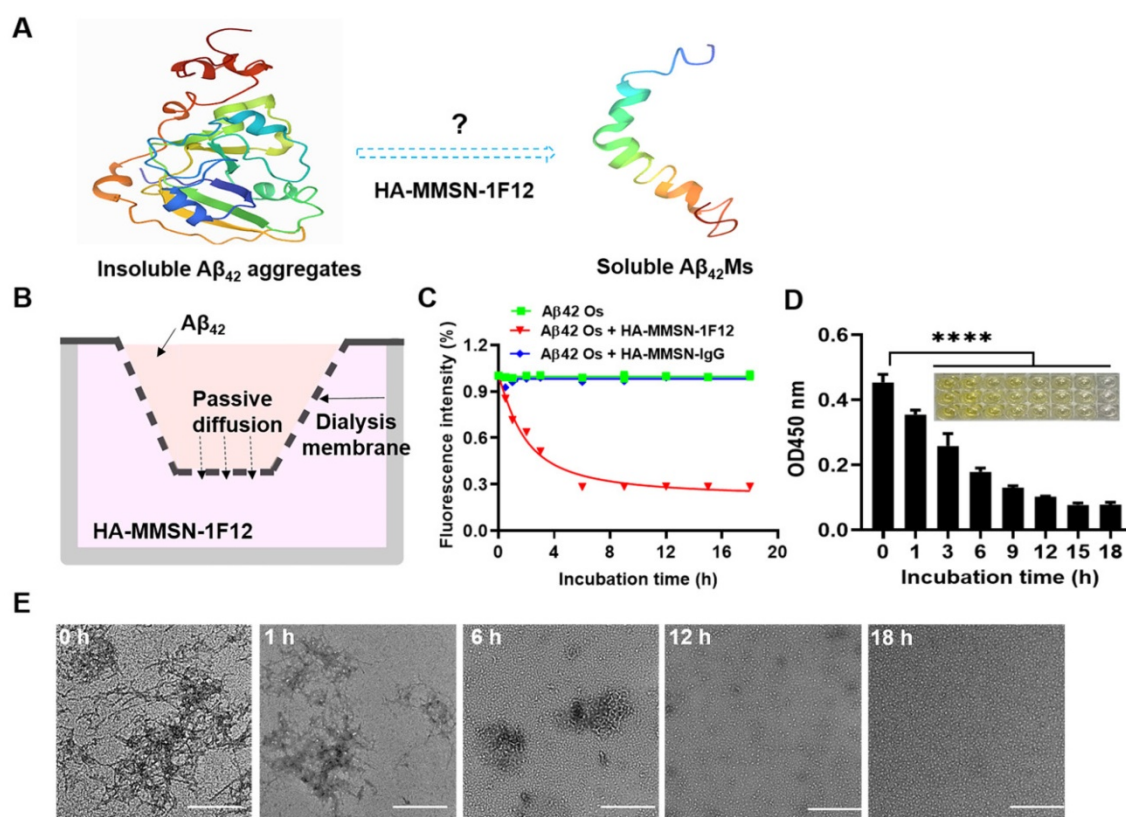


Figure 2. Evaluating the effect of HA-MMSN-1F12 on Aβ₄₂ aggregate degradation. (A) Schematic diagrams of degrading Aβ₄₂ aggregates to monomers. (B) Construction of an *in vitro* Aβ₄₂ aggregate degradation system using the transwell system. (C) The degradation kinetics of Aβ₄₂Os in the upper chamber under the HA-MMSN-1F12 or HA-MMSN-IgG action in the lower chamber was monitored through ThT fluorescence. (D) ELISA was used to monitor changes in the level of Aβ₄₂Os in the upper chamber under the action of HA-MMSN-1F12. (E) TEM images of Aβ₄₂ in the upper chamber when Aβ₄₂Os are in the upper chamber were incubated using HA-MMSN-1F12 in the lower chamber at 37 °C for 0, 1, 6, 12, and 18 h. Scale bar, 500 nm.

Assessing the ability of HA-MMSN-1F12 to depolymerize insoluble Aβ₄₂ aggregates

A system for degrading Aβ₄₂ aggregates *in vitro* was constructed to investigate whether HA-MMSN-1F12 could degrade Aβ₄₂ aggregates into monomers. If Aβ₄₂ aggregates in the upper chamber can be depolymerized into monomers, due to the difference in Aβ₄₂ concentration, Aβ₄₂ monomers (Aβ₄₂Ms) will be transferred to the lower chamber and captured by HA-MMSN-1F12 (Figure 2A-B). In addition, ThT fluorescence and ELISA assays were performed to quantify changes in Aβ₄₂ oligomers (Aβ₄₂Os) levels in the upper chamber after different treatments. The results showed that the ThT fluorescence intensity in the upper chamber of the HA-MMSN-1F12-treated group was significantly lower than that of the HA-MMSN-IgG-treated group (Figure 2C), which was consistent with the ELISA results (Figure 2D). This indicated that Aβ₄₂Os in the upper chamber were continuously dissociated into Aβ₄₂Ms under the action of HA-MMSN-1F12 in the lower chamber, resulting in a gradual decrease in the level of Aβ₄₂Os in the upper chamber.

Next, the morphological changes of Aβ₄₂ aggregates disaggregated in the upper chamber at

different times under the action of HA-MMSN-1F12 in the lower chamber were confirmed by TEM. Figure 2E shows that under the action of HA-MMSN-1F12, the number of Aβ₄₂ aggregates in the upper chamber continued to decrease and the number of Aβ₄₂Ms gradually increased. After more than 18 h of incubation with HA-MMSN-1F12 in the lower chamber, only Aβ₄₂Ms were present in the upper chamber. In addition, HA-MMSN-1F12 also inhibited the self-assembly of Aβ₄₂ aggregates (Figure S6). Therefore, HA-MMSN-1F12 could promote the disaggregation of Aβ₄₂ aggregates and inhibit their self-assembly.

Evaluation of brain delivery efficiency and intestinal metabolism of HA-MMSN-1F12

HUVECs were incubated with Cy3-labeled 1F12, HA-MMSN-1F12, HA-MMSN, and MMSN in the upper chamber at 37 °C for 24 h to investigate their uptake by SY5Y cells in the lower chamber. Confocal imaging revealed a robust Cy3 signal detectable in SY5Y cells in the HA-MMSN and HA-MMSN-1F12-treated groups (Figure 3A). This indicated that HA could facilitate the passage of its conjugated nanoparticles through vascular endothelial cells. In

addition, CD44 was highly expressed in ten-month-old APP/PS1 brains (Figure S8), which was more favorable for helping HA-MMSN-1F12 to cross the BBB.

Next, the efficiency of intravenous injection of HA-MMSN-1F12 across the BBB was investigated. APP/PS1 transgenic mice are an age-dependent developmental AD mouse model for brain A β deposition. After intravenous injection of Cy5-labeled 1F12, HA-MMSN-1F12, HA-MMSN, and MMSN in APP/PS1 mice, organ fluorescence imaging revealed strong fluorescence signals in the brains of mice treated with Cy5-labeled HA-MMSN and HA-

MMSN-1F12 after 3 h of injection. In contrast, no signal was detected in the MMSN- and 1F12-treated groups (Figure 3B). Quantitative analysis of homogenized brain tissue revealed efficient accumulation of Cy5-labeled HA-MMSN-1F12 in the brain over time. Signals detected in the brain were 1.12 ± 0.08 and 1.57 ± 0.06 %ID/g at 3 and 6 h post-injection, respectively (Figure 3C). However, only 0.32 ± 0.10 and 0.51 ± 0.07 %ID/g signals were detected at 3 and 6 h post-injection for 1F12-treated mice, significantly lower ($p < 0.0001$) than those in HA-MMSN-1F12-treated mice, indicating that HA facilitates its conjugate across the BBB.

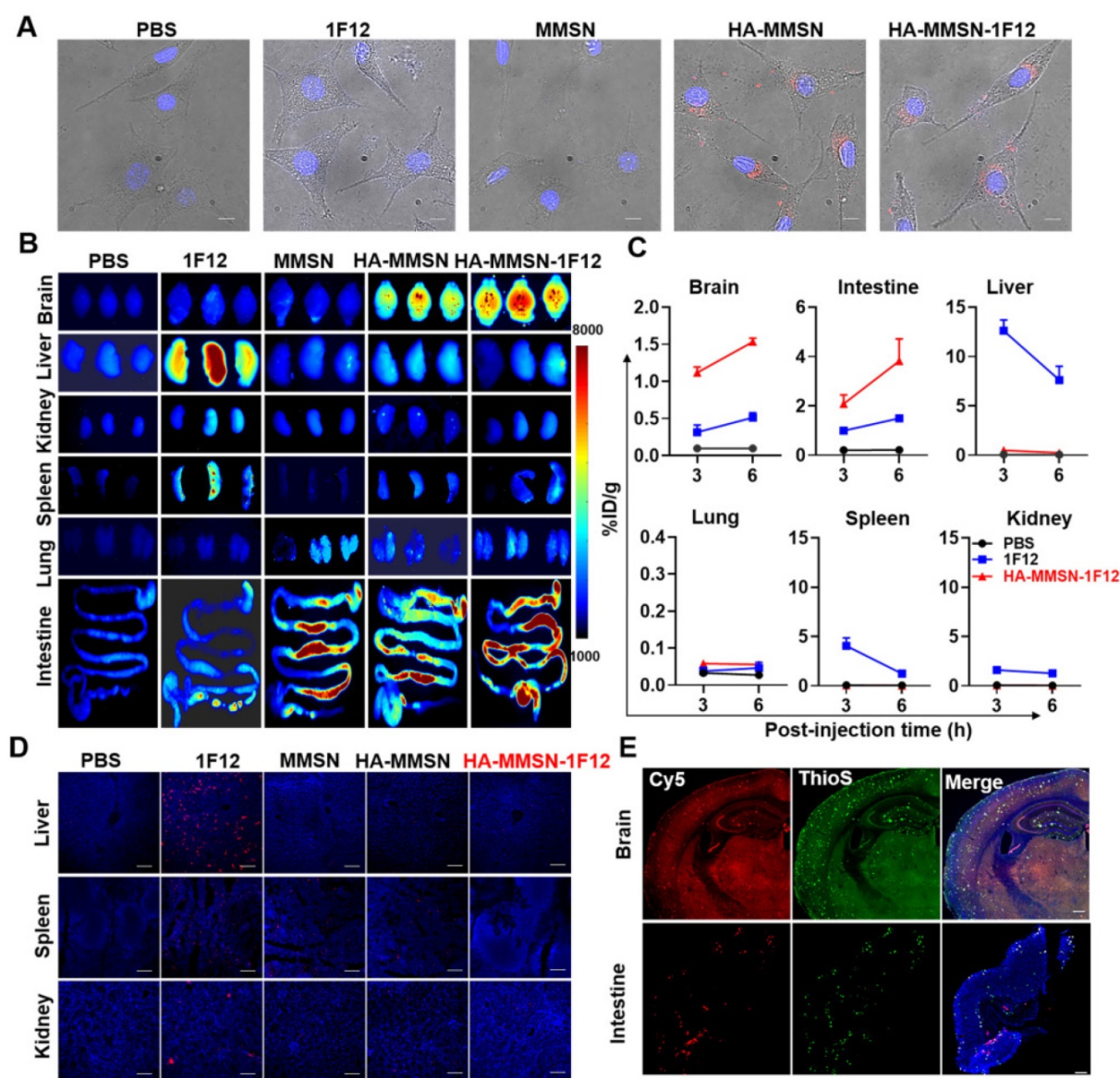


Figure 3. Evaluation of brain delivery efficiency and intestinal metabolism of HA-MMSN-1F12. (A) Confocal imaging of the SH-SY5Y cells in the transwell system and pretreated using Cy3-labeled 1F12, MMSN, HA-MMSN-1F12, or HA-MMSN in the upper chamber for evaluating the ability of these fluorescent probes to enter the brain. DAPI (blue), Cy3 (red), and scale bar, 200 μ m. (B) Fluorescence imaging of the organs from ten-month-old APP/PS1 mice at 3 h post-injection of the Cy5-labeled 1F12, MMSN, HA-MMSN-1F12, and HA-MMSN. $n = 3$ per group. (C) Quantitative analysis of the organs homogenates from ten-month-old APP/PS1 mice at 3 and 6 h post-injection of Cy5-labeled 1F12, MMSN, HA-MMSN-1F12, and HA-MMSN. $n = 3$ per group. (D) Confocal imaging of liver, spleen, and kidney tissue sections from eight-month-old APP/PS1 mice at 3 h p.i. of Cy5-labeled 1F12, MMSN, HA-MMSN-1F12, and HA-MMSN; DAPI (blue), Cy5 (red), and the scale bar, 100 μ m; $n = 3$ per group. (E) Confocal imaging of the brain and intestinal tissue sections from the ten-month-old APP/PS1 mice at 6 h post-injection of Cy5-labeled HA-MMSN-1F12. DAPI (blue), Cy5 (red), ThioS (green), and scale bar, 200 μ m. $n = 3$ per group.

In addition, organ fluorescence imaging depicted a strong fluorescence signal in the liver of mice treated with Cy5-labeled 1F12 at 3 h post-injection. In contrast, no signal was detected in the MMSN- and PBS-treated groups (Figure 3B). According to a quantitative analysis of homogenized liver tissues, 12.60 ± 1.11 %ID/g and 7.62 ± 1.40 %ID/g signals were detected in mouse livers after 3 and 6 h post-injection of 1F12, respectively (Figure 3C). In contrast, only 0.07-0.50 %ID/g signal was detected in the liver of mice in the HA-MMSN-1F12-treated group, and the low liver uptake of HA-MMSN-1F12 was further confirmed by confocal imaging of tissue slices (Figure 3D). Furthermore, fluorescence imaging also revealed that Cy5-labeled MMSN, HA-MMSN, and HA-MMSN-1F12 were rapidly metabolized in the intestine after 3 h of injection, but not Cy5-1F12 (Figure 3B and Figure S9A). The uptake of

Cy5-HA-MMSN-1F12 in the colon was 3.82 ± 0.89 %ID/g after 6 h of injection, which was significantly higher ($p < 0.0001$) than that of Cy5-1F12 (1.50 ± 0.11 %ID/g; Figure 3C and Figure S9A). This may be due to the shorter blood half-life of MMSN-based probes than Cy5-1F12 (Figure S9B). In addition, 3 h after intravenous administration of Cy5-HA-MMSN-1F12, weak fluorescence signals were also observed in the spleen, lung, and kidney of mice (Figure 3B-C). Immunofluorescence imaging of tissue sections revealed that the Cy5 fluorescence signal of HA-MMSN-1F12 but not HA-MMSN colocalized with the ThioS signal in the brain and small intestine (Figure 3D and Figure S10). The signals indicated that intravenously injected HA-MMSN-1F12 could specifically label A β in the brain via the BBB and that HA-MMSN-1F12 metabolized in the intestine could also target intestinal A β .

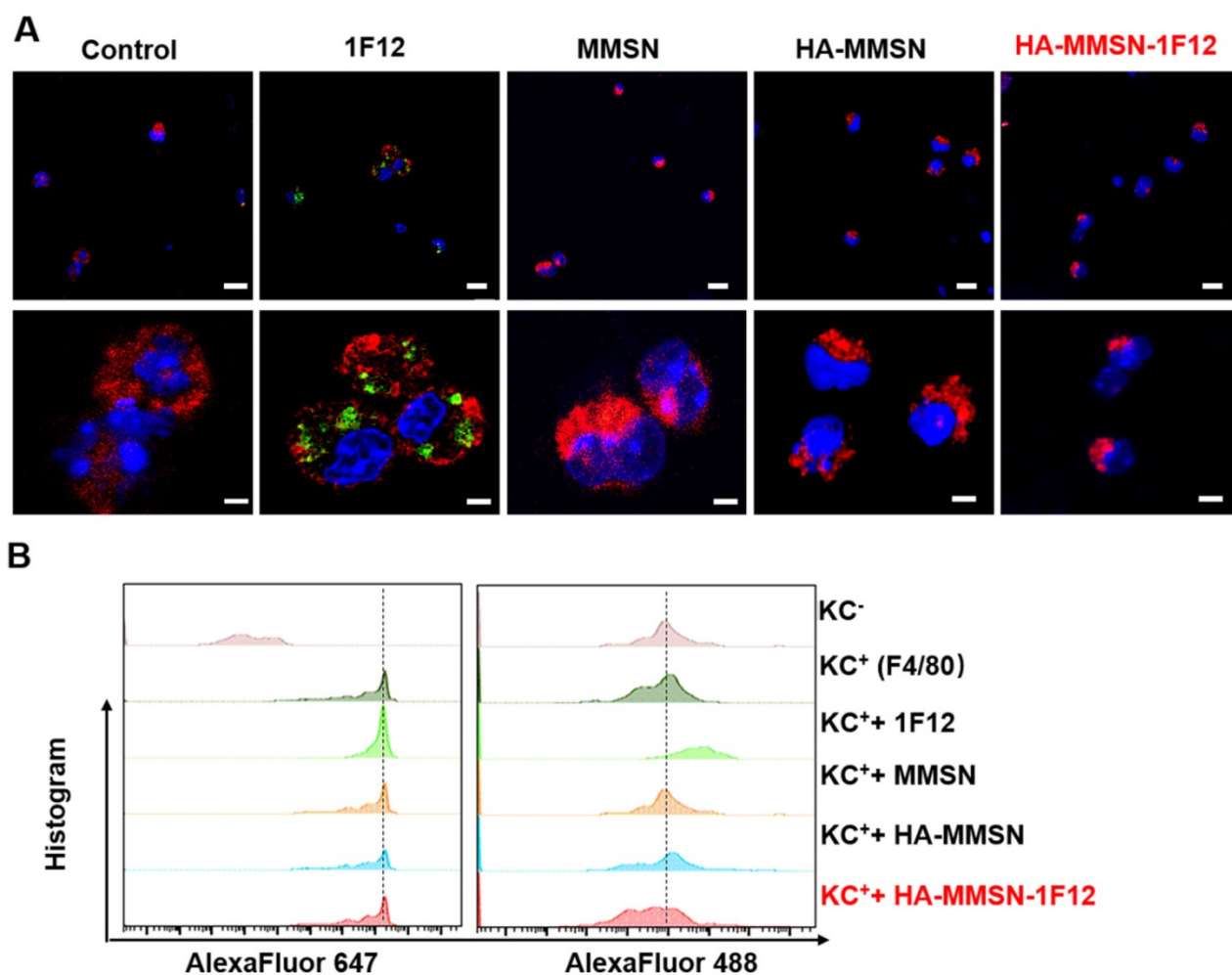


Figure 4. Escape from the uptake of HA-MMSN-1F12 through KCs. **(A)** Confocal imaging of KCs after 2 h incubation through the Alexa Fluor 488-labeled 1F12, MMSN, HA-MMSN-1F12, and HA-MMSN. **(B)** Representative flow cytometry histograms of KCs (F4/80-Alexa Fluor 647-positive) absorbed Alexa Fluor 488-labeled 1F12, MMSN, HA-MMSN-1F12, and HA-MMSN; DAPI (blue), F4/80-Alexa Fluor 647 (red), Alexa Fluor 488 (green). One-way analysis of variance (ANOVA) was utilized to undergo multigroup comparisons.

Escape of HA-MMSN-1F12 uptake by Kupffer cells

Kupffer cells (KCs) are resident hepatic macrophages responsible for the phagocytosis of circulating pathogens and exogenous nanomaterials. Next, the underlying mechanism leading to the good performance of HA-MMSN-1F12 was investigated. Alexa Fluor488-labeled 1F12, MMSN, HA-MMSN, and HA-MMSN-1F12 were incubated using Alexa-Fluor 647-F4/80 positive KCs (F4/80⁺-KCs) to understand the low liver absorption rate of HA-MMSN-1F12, marked as F4/80 to ensure primary KCs [33]. Flow cytometry and confocal imaging showed that F4/80⁺-KC mainly occupied 1F12. In contrast, the uptake of MMSN, HA-MMSN, and HA-MMSN-1F12 by F4/80⁺-KC was negligible, suggesting that HA-MMSN-1F12 could avoid the uptake of KCs (Figure 4). This is extremely important in the clearance of peripheral A β ₄₂ by altering the metabolic pathway of circulating A β ₄₂ in the intestine.

Evaluating the effect of HA-MMSN-1F12 on A β ₄₂ clearance in peripheral blood

Intravenously injected HA-MMSN-1F12 could target and depolymerize A β brain plaques as monomers through the BBB and peripheral efflux. In contrast, all peripheral A β ₄₂ species would be captured by HA-MMSN-1F12 and excreted through intestinal metabolism, thereby reducing A β burden within the brain (Figure 5A). Mouse blood was incubated with protein A columns to enrich HA-MMSN-1F12 complexes and circulating A β ₄₂ 12 h after post-injection of HA-MMSN-1F12 to evaluate whether 4 mg/kg of HA-MMSN-1F12 could be an effective treatment dose. Western blotting results showed that distinct A β ₄₂O_s bands were observed in protein A beads, but not in the protein A elution solution, indicating that HA-MMSN-1F12 captured all free A β ₄₂ in the blood (Figure S11A). Therefore, HA-MMSN-1F12 behaves as a sink for A β ₄₂ in the blood, and an intravenous dose of 4 mg/kg of HA-MMSN-1F12 can effectively bind all A β ₄₂ species.

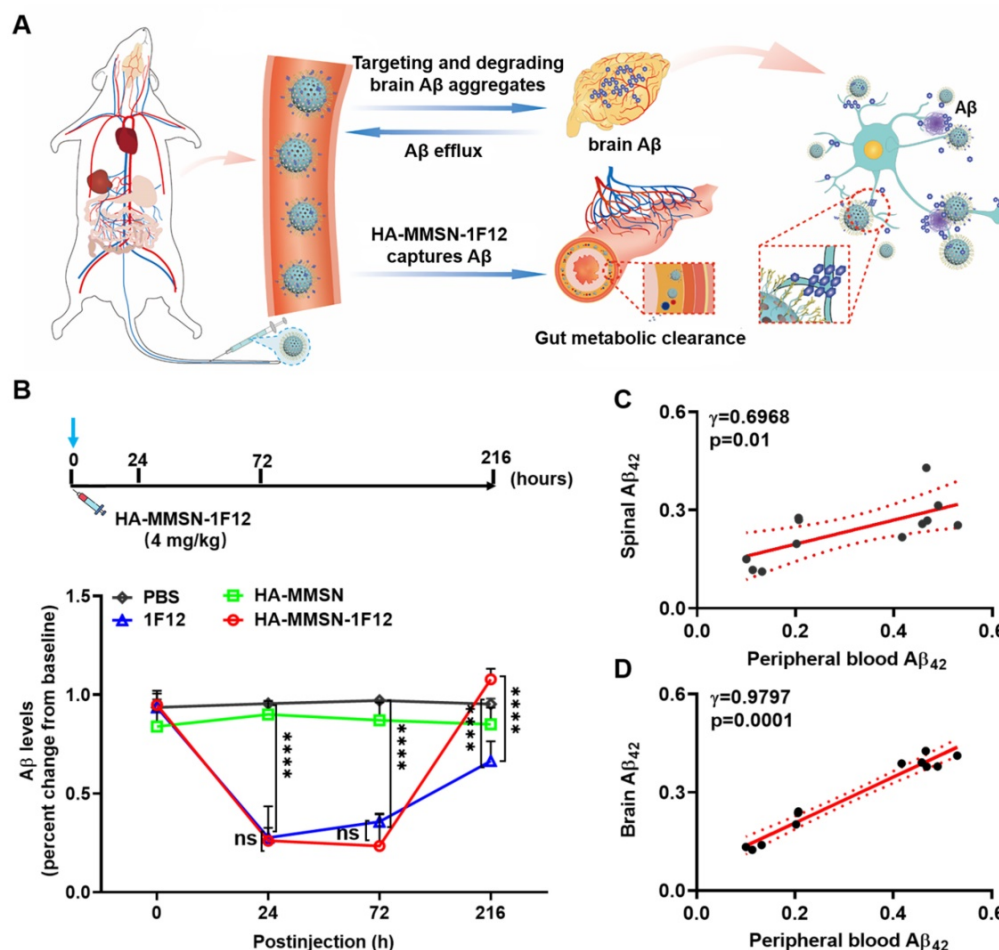


Figure 5. A β clearance after the intravenous administration of HA-MMSN-1F12. (A) Schematic illustrations of the A β burden reduction within the brain by intravenously injecting HA-MMSN-1F12. Intravenously injected HA-MMSN-1F12 crossed the blood-brain barrier into the brain for degrading insoluble A β aggregates into soluble monomers and flowing into the periphery. Similarly, peripheral soluble A β was captured using HA-MMSN-1F12 and excreted using intestinal metabolism, thereby reducing the brain A β burden. (B) Changes in the peripheral blood of A β levels in ten-month-old APP/PS1 mice after single-dose intravenous injection of HA-MMSN, 1F12, and HA-MMSN-1F12. The correlation between changes in A β levels in peripheral blood and spinal cord (C) or brain (D) (Pearson correlation). $n = 3$ per group. One-way analysis of variance (ANOVA) was performed to undergo multiple group comparisons. Statistical significance is considered with *** $p < 0.001$, and n.s. (indicating no significance).

Next, the effect of HA-MMSN-1F12 on $A\beta_{42}$ clearance in peripheral blood and the dynamic interaction between peripheral and central $A\beta_{42}$ levels was also investigated. Ten-month-old male APP/PS1 mice with the closest positive serum OD450 values were selected for the experiments to reduce errors due to differences between mice (Figure S11B). After a single intravenous dose of HA-MMSN-1F12, a decrease in peripheral $A\beta_{42}$ levels was observed, reaching a minimum level 24 h after post-injection ($p < 0.0001$). Furthermore, it gradually increased and reached near baseline levels (Figure 5B). In contrast, $A\beta_{42}$ levels in the blood of mice treated with HA-MMSN and PBS did not change significantly. Moreover, intravenous administration of 1F12 significantly reduced $A\beta_{42}$ levels in peripheral blood. Peripheral blood $A\beta_{42}$ levels at 24 h ($p = 0.9943$) and 72

h ($p > 0.1836$) after post-injection were not significantly different from the HA-MMSN-1F12-treated group. However, peripheral blood $A\beta_{42}$ levels in HA-MMSN-1F12-treated mice recovered significantly faster than in the 1F12-treated mice ($p < 0.0001$) and exceeded baseline levels ($p = 0.2061$) 216 h after injection (Figure 5B). In addition, regression analysis showed that soluble $A\beta_{42}$ blood levels were positively correlated with those in the spinal cord ($r = 0.6968$; Figure 5C) and brain ($r = 0.9797$; Figure 5D), implying that more soluble $A\beta_{42}$ was produced in the brain at 216 h post-injection. These results indicated that HA-MMSN-1F12 could enter the brain to depolymerize $A\beta$ plaques and form more soluble $A\beta$ to flow into the periphery, increasing peripheral blood $A\beta$ levels.

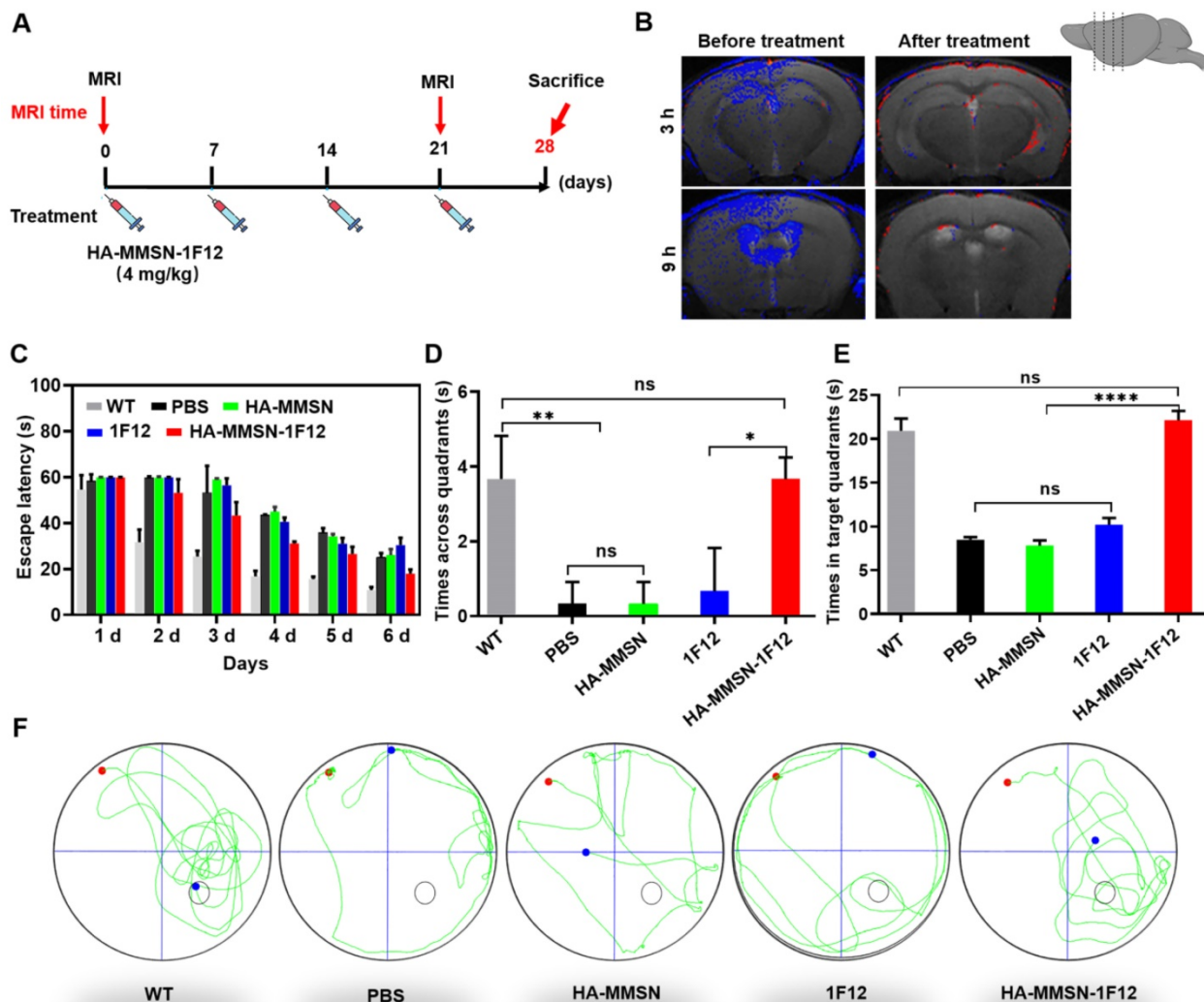


Figure 6. HA-MMSN-1F12 improves cognitive impairment. (A) Schematic diagram showing the treatment of ten-month-old APP/PS1 mice through intravenous injection of HA-MMSN-1F12; $n = 3$ per group. **(B)** Magnetic resonance imaging of the brain 3 and 9 h post-injection of HA-MMSN-1F12 in ten-month-old APP/PS1 mice pretreated with either 4 mg/kg HA-MMSN-1F12 or PBS for three weeks. **(C)** Escape latency to the platform during the training phase. **(D)** Platform entries. **(E)** Time spent within the target quadrant. **(F)** Representative swimming paths of mice within the probe test. Two-way analysis of variance (ANOVA) was performed to undergo multigroup comparisons. Statistical significance is indicated with * $p < 0.05$, ** $p < 0.01$, **** $p < 0.0001$, and n.s. (no significance).

Intravenous administration of HA-MMSN-1F12 improves cognitive deficits

We performed MRI by intravenous injection of HA-MMSN-1F12 into ten-month-old APP/PS1 mice pretreated with HA-MMSN-1F12 for three weeks to evaluate its therapeutic effect (4 mg/kg/week; Figure 6A). PBS was used as a control, and brain MRI was performed 3 and 9 h after post-injection of HA-MMSN-1F12. Results showed robust T2 MRI signals (blue) in the cortex and hippocampus of APP/PS1 mice. In contrast, T2 MRI signals were weaker in APP/PS1 mice treated with HA-MMSN-1F12 (Figure 6B), indicating that HA-MMSN-1F12 significantly reduced A β plaques in the brains of APP/PS1 mice.

AD is a progressive neurodegenerative disease that results in progressive cognitive impairment. We studied whether intravenous administration of HA-MMSN-1F12 could effectively improve cognitive deficits based on MRI results. Next, the Morris water maze test evaluated the effect of HA-MMSN-1F12 on cognitive deficits in APP/PS1 mice. Compared to WT mice, APP/PS1 mice took longer to reach the underwater platform during training trials (Figure 6C) and made fewer crossings inside the target zone of the underwater platform (Figure 6D). In addition, they swam less in the target quadrant on the sixth day (Figure 6E), indicating significant spatial memory deficits. Notably, HA-MMSN and 1F12 treatments failed to statistically improve memory function compared to control APP/PS1 mice (Figure 6D-F). However, *t* learning and memory abilities were significantly improved after HA-MMSN-1F12 administration (Figure 6D-F). Furthermore, HA-MMSN-1F12-treated APP/PS1 mice exhibited spatially oriented swimming behavior (Figure 6F).

Assessing the effect of HA-MMSN-1F12 on reducing brain A β burden

We investigated whether intravenous administration of HA-MMSN-1F12 reduces brain A β . HA-MMSN-1F12-treated mice had significantly lower ThioS-positive A β plaques in the cortex ($p < 0.0009$) and hippocampus ($p < 0.0001$) than PBS-treated mice (Figure 7A and Figure S12). The number of A β plaques in the cortex ($p = 0.0013$) and hippocampus ($p = 0.0303$; Figure 7B) of mice treated with HA-MMSN-1F12 was significantly reduced compared to mice treated with 1F12.

Next, we investigated whether intravenous injection of HA-MMSN-1F12 could inhibit microglial activation. The area fraction of CD86-positive microglia in the cortex and hippocampus was significantly

reduced ($p < 0.0001$) in HA-MMSN-1F12- and 1F12-treated mice compared to PBS-treated mice (Figure S13A-B). In addition, the number of CD86-positive microglia in the cortex ($p = 0.0379$) was significantly lower than that in 1F12-treated mice, but not in the hippocampus ($p = 0.1828$) of HA-MMSN-1F12-treated mice. Blockade of microglial activation in AD models has been found to be neuroprotective [34], and massive A β accumulation is accompanied by local microglial activation [35]. Therefore, the interaction between microglia and A β was further investigated. Immunofluorescence staining of the cerebral cortex of PBS-treated mice showed swelling of microglia, branching cells with larger cell bodies and shorter protrusions, and activated microglia surrounded by extensive A β plaques (Figure 7C and Figure S14), consistent with previous findings [36, 37]. HA-MMSN-1F12-treated mice had more small A β plaques and microglia with quiescent branching morphology. 1F12-treated mice exhibited a similar phenomenon, which was not as pronounced as HA-MMSN-1F12-treated mice (Figure 7C). Quantitative analysis revealed that HA-MMSN-1F12-treated mice had the longest microglia body diameter ($p < 0.0001$) and the highest resting cell number ($p < 0.0001$) in the cortex (Figure 7C) than PBS-treated mice. Moreover, regression analysis revealed that the diameter of cell bodies depended on the size of A β plaques (Figure 7C). Therefore, these results confirmed that HA-MMSN-1F12 reduced A β plaque burden in the brain by depolymerizing and blocking microglial activation.

Next, we investigated whether intravenous administration of HA-MMSN-1F12 could attenuate neuroinflammation. The levels of the anti-inflammatory cytokines interleukin 2 (IL-2) and interleukin 4 (IL-4) were significantly increased in HA-MMSN-1F12-treated mice ($p < 0.0001$; Figure 7D) compared to PBS-treated mice. However, intravenous administration of HA-MMSN-1F12 significantly increased IL-2 ($p = 0.0016$), IL-4 ($p < 0.0001$) and interleukin 10 (IL-10) ($p < 0.0001$) compared to the 1F12-treated mice (Figure 7D). Furthermore, HA-MMSN-1F12 significantly decreased the pro-inflammatory cytokine interleukin 6 (IL-6) compared with PBS ($p = 0.0002$), MMSN ($p = 0.0053$), and 1F12 groups ($p = 0.0073$; Figure 7E). Tumor necrosis factor- α (TNF- α) and interferon- γ (IFN- γ) levels were not significantly affected in all treatment groups. Therefore, intravenously injected HA-MMSN-1F12 significantly increased anti-inflammatory factors and decreased the levels of pro-inflammatory factor IL-6 in the brain.

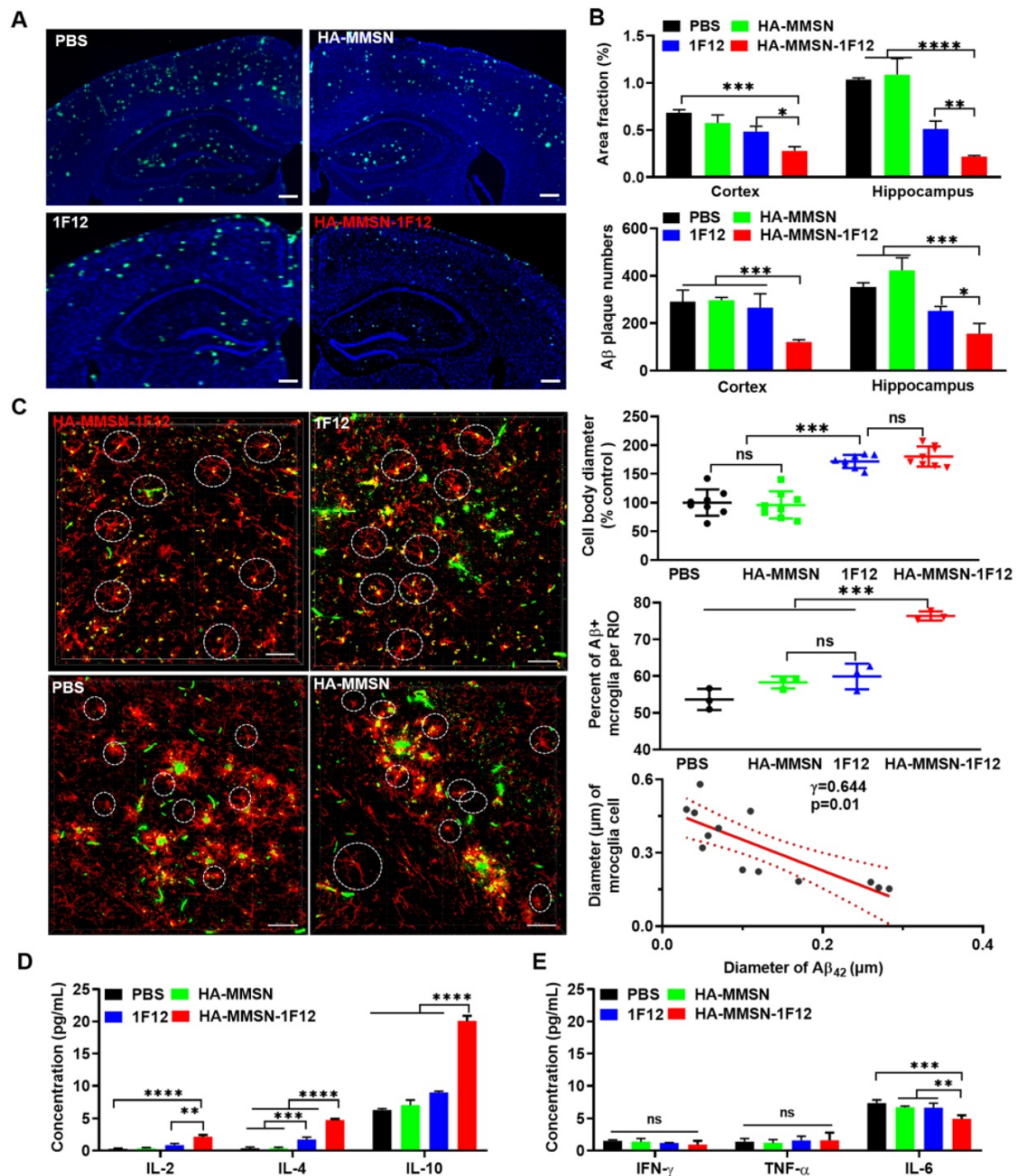


Figure 7. Intravenous HA-MMSN-1F12 improves the Aβ burden and neuroinflammation in the brain. (A) Representative images of the brain sections using ThioS staining in ten-month-old APP/PS1 mice after treatment using PBS, HA-MMSN, 1F12, and HA-MMSN-1F12; n = 3 per group. ThioS (green) assessed the number of Aβ plaques after treatment; scale bar, 100 μm. (B) Area fraction and number of Aβ plaques in the hippocampus and cortex of ten-month-old APP/PS1 mice treated with PBS, HA-MMSN, 1F12, and HA-MMSN-1F12. (C) Representative images of microglia and Aβ plaques after immunostaining using anti-IBA1 and anti-Aβ (6E10) within the hippocampal CA1 region of ten-month-old APP/PS1 mice treated with PBS, HA-MMSN, 1F12, or HA-MMSN-1F12. Quantitative analysis of the diameter of IBA1-positive microglial cell bodies, the percentage of Aβ-positive microglia (white cycle), and the correlation between the diameter changes of IBA1-positive microglial cell bodies and the Aβ plaque diameter (Pearson's correlation) from ten-month-old APP/PS1 mice treated with PBS, HA-MMSN, 1F12, or HA-MMSN-1F12. IBA1 (red), 6E10 (green), and scale bar, 500 μm. Quantitative analysis expressing (D) anti-inflammatory factors (IL-2, IL-4, and IL-10) and (E) pro-inflammatory factors (IFN-γ, TNF-α, and IL-6). Two-way analysis of variance (ANOVA) was undergone for multigroup comparisons. Statistical significance is considered when *p < 0.05, **p < 0.01, ***p < 0.001, ****p < 0.0001, and n.s (indicating no significance).

Then, the underlying mechanisms of reducing brain Aβ burden and attenuating neuroinflammation after intravenous injection of HA-MMSN-1F12 were explored. Transcriptomic analysis of the hippocampus of the three groups identified a series of differentially expressed genes (DEGs) (Figure S15). Among the down-regulated DEGs, HA-MMSN-1F12-treated mice depicted lower expression levels of

mitochondrially encoded ATP synthase membrane subunit 6 (mt-Atp6) and subunit 8 (mt-Atp8) than 1F12- and HA-MMSN-treated mice (Figure S15). This suggests that HA-MMSN-1F12 can ameliorate mitochondrial dysfunction in APP/PS1 mice, an early event in AD pathogenesis due to progressive accumulations of mitochondrial Aβ [38]. Transcriptome results from the two groups were compared for the

unequivocal discovery of variable genes. Transcriptomes of HA-MMSN-1F12- and 1F12-treated mice showed 140 up-regulated and 291 down-regulated genes. In contrast, the transcriptomes of HA-MSN-1F12- and HA-MMSN-treated mice showed 113 up-regulated genes and 165 down-regulated genes (Figure S16A). Hierarchical cluster analysis of DEGs showed that transcriptomic profiles could effectively distinguish samples from the two treatment groups, indicating different expression patterns within the treatment groups (Figure S16 B-C). Next, KEGG pathway analysis was performed on the DEGs between the two groups. Based on enriched gene counts, several important signaling pathways were related to the immune system and its diseases, nervous system, and neurodegenerative diseases (Figure S17A-B). Finally, the DEG-based co-expression network identified a core node gene called tyrosine hydroxylase (Th), which plays an important role in dopamine synthesis (Figure S18). The down-regulated expression of Th directly affects the synthesis and secretion of dopamine. However, the down-regulation of Th gene and its association with AD pathology remains unclear.

Biosafety evaluation of HA-MMSN-1F12

According to previous reports, the complete degradation of conventional MMSN takes several weeks [39]. MMSN was optimized during synthesis, and its porosity was changed. Therefore, we tried to study its biodegradability. HA-MMSN-1F12 was incubated with simulated body fluid (Krebs-Henseleit solution) for 48 h at 37 °C. TEM showed rapid degradation of silica in HA-MMSN-1F12 (Figure S19A), confirming the excellent biodegradability of MMSN. In addition, HA-MMSN-1F12 was injected into eight-month-old C57BL/6 mice to evaluate the potential toxicity of HA-MMSN-1F12 *in vivo*, and the blood was collected for biochemical analysis. No measurable adverse effects were observed in liver (ALB, 22.33 ± 0.57 g/L; ALP, 143.33 ± 9.01 IU/L; and ALT, 38.00 ± 1.00 IU/L) and renal (BUN, 10.77 ± 0.46 mmol/L; CRE, 84.00 ± 4.36 μ mol/L; and GLOB, 32 ± 1.73 g/L) functions in HA-MMSN-1F12-treated mice (Figure S19B). In addition, no significant differences in histology were observed between HA-MMSN-1F12 and PBS controls. Moreover, no obvious pathological abnormalities were observed in the heart, liver, spleen, lung, and kidney (Figure S19C), indicating that HA-MMSN-1F12 has extremely high biosafety.

Discussion

This study reported a unique A β removal strategy based on large-sized multifunctional MMSN

with surface-coupled anti-A β_{42} mAb 1F12 that captures peripheral soluble A β_{42} and the brain CD44 ligand HA for enhanced brain entry efficiency. Intravenous administration of HA-MMSN-1F12 for three weeks significantly reduced brain A β burden, neuroinflammation, and cognitive deficits in APP/PS1 mice. HA-MMSN-1F12 could depolymerize insoluble A β aggregates into soluble A β monomers in the brain and excrete A β through the intestinal metabolic pathways.

Studies have observed that CD44 localizes to the lipid valve of cerebral vascular endothelial cells. Specific binding to the ligand HA induces the synthesis of downstream protein kinase C- α (PKC- α). Thus, the reorganization of the cerebrovascular endothelial cytoskeleton and the formation of pseudopodia are triggered to exert their phagocytic function into the brain [40-42]. Notably, CD44 was also highly expressed in the brains of APP/PS1 mice (Figure S8). Therefore, the HA/CD44 interaction may be a potential target of the entire BBB for AD therapy. In addition, HA facilitated the passage of its conjugate MMSN-1F12 through vascular endothelial cells via an *in vitro* BBB model (Figure 3A). Furthermore, *in vivo* experiments showed that intravenously injected HA-MMSN-1F12 was present in the brain of APP/PS1 mice up to 1.57 ± 0.06 %ID/g and specifically labeled A β_{42} in the brain (Figure 3B-E). Our findings suggest that HA can assist drugs in crossing the BBB and be used to treat neurological disorders. After intravenous administration of HA-coupled MMSN-1F12, brain A β levels and neuroinflammation were significantly reduced in APP/PS1 mice, with improved cognitive function (Figures 6 and 7). In addition, HA-MMSN-1F12 was rapidly degraded after 48 h (Figure S19A), suggesting the safety and efficacy of HA-MMSN-1F12 in clearing central A β .

The liver sequesters up to 70% of nanomaterials and only 0.7% is delivered to the target [43], resulting in inefficient drug delivery and poor therapeutic efficacy. Studies have depicted a clear correlation between macrophage uptake and efficient targeted delivery [44, 45]. The physicochemical properties of nanomaterials, such as size, shape, charge, and "stealth" surface, affect their interaction with macrophages and blood half-life [46, 47]. Within a certain size range, the larger the particle size of spherical nanomaterials, the easier they are to be internalized by macrophages [48]. In this study, the low enrichment of HA-MMSN-1F12 in the liver was associated with its non-sphericity (Figure 1B-C). In addition, HA is very hydrophilic, so HA-MMSN-1F12 has a high negative charge (-13.03 ± 0.12 mV). It could help HA-MMSN-1F12 avoid interacting with opsonins, thereby reducing the accumulation of

macrophages (Figures 3 and 4). The hepatic uptake was low at 3 h after intravenous injection of 4 mg/kg HA-MMSN-1F12, only 0.07-0.50 %ID/g in the liver, indicating that the large particle size of HA-MMSN-1F12 can escape the uptake of hepatic KCs (Figure 3 and 4). Therefore, the characteristic physicochemical properties of HA-MMSN-1F12 can increase the concentration of HA-MMSN-1F12 in peripheral blood and improve its efficiency across the BBB in the brain.

A β levels in the central nervous system are 20 to 67 times higher than in the periphery. A β levels in the brains AD mice can increase by more than 30% within three months [49]. However, clinical results indicate that intravenous infusion of A β antibodies has limited effect in reducing A β burden in the brain. In the current study, peripheral blood A β_{42} levels reached a minimum at 24 h and increased again at 216 h, higher than baseline after a single intravenous injection of HA-MMSN-1F12 (Figure 5B). Blood soluble A β_{42} levels were positively correlated with brain A β levels. Thus, peripheral blood A β_{42} levels were higher than baseline at 216 h, indicating elevated brain soluble A β_{42} levels. *In vitro* simulation experiments confirmed that HA-MMSN-1F12 could degrade A β_{42} aggregates into soluble A β_{42} species (Figure 2). Furthermore, 1F12 and HA-MMSN-1F12 showed no significant difference in reducing A β_{42} levels in peripheral blood. The immunofluorescence results of brain sections showed that the A β plaques in the brains of mice in the HA-MMSN-1F12 treatment group were smaller than those in the 1F12 treatment group (Figure 7). Targeting the depolymerization of A β plaques in the brain and the rapid excretion of peripheral soluble A β by intestinal metabolism is characterized by the excellent therapeutic effect of HA-MMSN-1F12 in reducing the A β burden in the brain.

The clinical diagnosis of AD includes positron emission tomography (PET) and cerebrospinal fluid (CSF) detection [50, 51]. PET is expensive and radioactive, while CSF is invasive. MRI is not invasive and radioactive and less expensive than PET scanning but lacks A β -specific MRI probes [52, 53]. The development of A β -specific MR probes is significant for the diagnosis of AD. The developed HA-MMSN-1F12 showed high binding affinity ($K_d = 1.27 \pm 0.34$ nM) to A β_{42} Os *in vitro* (Figure 1D). In addition, the HA-MMSN-1F12 probe enables specific MR imaging of A β plaques in the brains of APP/PS1 mice to understand the pathological development of AD (Figure 6B), providing an excellent MRI probe value for AD diagnosis. HA-MMSN-1F12 MRI can identify structural information and molecular target locations during early A β accumulation. Therefore, HA-MMSN-1F12 has the potential to evaluate drug

candidate efficacy and early diagnosis of AD.

As a major player in neuroinflammation, microglia are crucial for the initiation and development of AD [54]. Most studies enhance A β clearance by activating microglia [55]. However, activation of microglia releases pro-inflammatory cytokines that further exacerbate inflammation, which in turn enhances A β production and neuroinflammation, leading to neuronal degeneration and necrosis. In this study, when A β plaques in the brain were cleared by HA-MMSN-1F12, the number of activated microglia decreased, generating more microglia with quiescent branching morphology (Figure 7), which resulted in the amelioration of cognitive deficits in AD mice (Figure 6). In addition, intravenous administration of HA-MMSN-1F12 increased the production and release of inflammatory cytokines, including IL-2, IL-4, and IL-10, resulting in anti-inflammatory responses (Figure 7D), promoting the improvement of neuroinflammation in AD. Therefore, restoring the physiological functions of microglia to alleviate neuroinflammation is also the key to AD treatment.

Based on the previously developed anti-A β_{42} mAb 1F12, we demonstrate that HA-MMSN-1F12, obtained by modifying the MMSN surface with HA and 1F12, reduces brain A β burden and neuroinflammation, and improves cognitive deficits in APP/PS1 mice. The superior efficacy of HA-MMSN-1F12 is related to its design, including 400-600 nm non-spherical particles and injectable doses to reduce hepatic clearance and degrade A β aggregates in the brain into soluble A β_{42} species that are excreted through intestinal metabolism. This study provides a new strategy to overcome off-target nanomaterial accumulation in the liver and excrete disease-causing biohazards through intestinal metabolism, providing a new therapeutic avenue for combating brain diseases.

Materials and methods

Chemicals and materials

A β_{40} , A β_{42} , and A β_{42} Arc peptides were lyophilized powders custom-synthesized from Royo Biotech Co., Ltd (Shanghai, Chian), with a purity of > 95%. Anti-A β (6E10) and Anti-CD86 antibodies were obtained from Invitrogen (Carlsbad, CA, USA). Anti-Iba1 (019-19741) was acquired from Wako laboratory chemicals (Osaka, Japan). An anti-CD44 antibody was obtained from Sevier Bio (Wuhan, China). Goat anti-mouse IgG (H+L) and protein A resin were ordered from GenScript (Nanjing, China). Pierce streptavidin-coupled Poly-Horseradish Peroxidase (HRP) and protein marker were purchased from Thermo Fisher Scientific. Thioflavin T (ThioT),

Thioflavin S (ThioS), Dimethyl sulfoxide (DMSO), and bovine serum albumin (BSA) were ordered from Sigma-Aldrich. N-hydroxysuccinimide (NHS) ester and Cy5-NHS ester were purchased from Lumiprobe (Hannover, Germany). $\text{FeCl}_2 \cdot 4\text{H}_2\text{O}$ was provided by Ourchem (Zhejiang, China). 4',6-diamidino-2-phenylindole (DAPI) was ordered from Beyotime Biotechnology (Shanghai, China). $\text{FeCl}_3 \cdot 6\text{H}_2\text{O}$ was provided by Lingfeng Chemical Reagents (Shanghai, China). 1-(3-Dimethylaminopropyl)-3-ethyl carbodiimide hydro (EDC), NHS (98%), Oleic acid (OA, AR), hyaluronic acid (HA), N-cetyltrimethylammonium bromide (CTAB, 99%), Ethyl acetate (EtOAc, 99.5%) and methanol were purchased from Aladdin (Shanghai, China). Tetraethyl orthosilicate (TEOS, 98%) was obtained from Macklin (Shanghai, China). All other chemicals were purchased from commercial suppliers and used as received.

Synthesis of magnetic mesoporous silica nanoparticles (MMSN)

Firstly, monodisperse superparamagnetic iron oxide nanoparticles coated with oleic acid ($\text{Fe}_3\text{O}_4@OA$) nanoparticles were prepared by the chemical co-precipitation technique [56]. Briefly, 33.5 mmol $\text{FeCl}_2 \cdot 4\text{H}_2\text{O}$ and 41.8 mmol $\text{FeCl}_3 \cdot 6\text{H}_2\text{O}$ were added to 80 mL of deionized water and heated to 80 °C under a nitrogen atmosphere. After vigorous stirring for 0.5 h, 45 mL of ammonium hydroxide and 2 mL of OA were added and reacted for 25 min to obtain $\text{Fe}_3\text{O}_4@OA$. Secondly, MMSN nanoparticles were synthesized using a sol-gel method with some modifications [57, 58]. 7.5 mg of $\text{Fe}_3\text{O}_4@OA$ was dissolved in 500 μL of chloroform and mixed with 0.1 g of CTAB in 5 mL of water. After vigorous stirring, a homogeneous oil-in-water microemulsion was obtained. After evaporating chloroform for 10 min at 60 °C, the resulting water-dispersed nanoparticles were diluted with 100 mL of water. Then, 22.70 mmol/L of ammonium hydroxide, 2.23 mmol/L of TEOS, and 51.10 mmol/L of EtOAc were added to the diluted aqueous solution containing magnetite nanoparticles. The resulting mixture was reacted for 30 s and centrifuged at 80 rpm to obtain MMSN.

Functional modification of HA-MMSN

The surface of MMSNs was modified with HA-NHS, that is, 10.8 $\mu\text{mol/L}$ HA was dissolved in 500 μL DMSO, and then 10.8 $\mu\text{mol/L}$ EDC and 54 $\mu\text{mol/L}$ NHS were added to the solution to activate HA. After adding activated HA-NHS to the MMSN solution for 3 h, the product was lyophilized to generate the corresponding HA-MMSN-NHS nanoparticles.

Conjugation of antibodies to HA-MMSNs-NHS was performed by using conventional amidation

reaction methods. Briefly, 10 nmol/L of the corresponding antibody (1F12 or IgG) was dissolved in 1 M PBS, adjusted to pH 8.5 with 0.1 M Na_2CO_3 , and then mixed with 20 nmol/L of HA-MMSN-NHS ester to react for 3-4 h at room temperature. Antibody-conjugated MMSNs were separated by a magnet to remove excess free antibodies. As shown in Figure S2C, representative FT-IR spectra of HA-MMSN-1F12 showed characteristic absorptions at 1653.90 and 3426.27 cm^{-1} (Amide I, HN-C=O stretching) and 1542.23 cm^{-1} correspond to $-\text{N-H}$ (Amide II) bending frequency, indicating that 1F12 has been successfully coupled to the surface of functionalized HA-MMSN-NHS.

Preparation of fluorescent dye-labeled 1F12 and HA-MMSN-1F12

Non-immune HA-MMSN-1F12 and 1F12 were conjugated to fluorescent dyes (Cy3-NHS or AlexaFluor 488) using the conventional amidation reaction chemistry method described above. Antibodies were stored at -80 °C before labeling with fluorochromes, and fluorochrome-labeled 1F12 were purified using a size-exclusion PD-10 column with 1 M PBS as mobile phase, and fluorochrome-conjugated HA-MMSN-1F12 were separated by a magnet to remove excess free fluorochrome. As shown in Figure S7, the results of fluorescence intensity and spectrum measurements showed that Cy3-labeled HA-MMSN-1F12 or 1F12 had strong Cy3 fluorescence intensity with a fluorescence peak at 561 nm, which indicated that Cy3 was successfully conjugated with HA-MMSN-1F12 or 1F12.

Preparation of oligomeric and monomeric A β

$A\beta_{40}$ monomers ($A\beta_{40}\text{Ms}$), $A\beta_{42}$ monomers ($A\beta_{42}\text{Ms}$), and $A\beta_{42}\text{Arc}$ monomers ($A\beta_{42}\text{ArcMs}$) were prepared by dissolving lyophilized $A\beta_{40}$, $A\beta_{42}$, and $A\beta_{42}\text{Arc}$ peptides in 10 mmol/L NaOH and diluted in 2 M phosphate-buffer saline. The prepared $A\beta_{40}$, $A\beta_{42}$, and $A\beta_{42}\text{Arc}$ monomers solutions (50 μM) were stored at -20 °C as stock solutions, respectively. $A\beta_{42}$ oligomers ($A\beta_{42}\text{Os}$) were obtained by dissolving lyophilized $A\beta_{42}$ peptide in 10 mmol/L NaOH and diluted to 50 μM in 10 M phosphate-buffer saline overnight at 37 °C in the dark. $A\beta_{42}\text{Arc}$ oligomers solution ($A\beta_{42}\text{ArcOs}$) was prepared by incubating its monomer for 1 h at 37 °C in the dark, followed by centrifugation at $17,900 \times g$ for 5 min.

Cryo-transmission electron microscopy

The patterns of the prepared $A\beta_{42}\text{Ms}$, $A\beta_{42}\text{ArcMs}$, $A\beta_{42}\text{Os}$ or $A\beta_{42}\text{ArcOs}$, HA-MMSN, and HA-MMSN-1F12 were confirmed by cryo-transmission electron microscopy (Cryo-TEM). Briefly, 5 μL of samples were dropped onto a copper grid, and excess

liquid was blotted with filter paper, leaving a thin film of solution on the mesh. The morphology of the above samples was characterized using a Tecnai G20 transmission electron microscope (FEI Ltd, USA). The instrument works in 80 kV and zero-loss bright field mode, showing as much detail as possible and enhancing image contrast at a focus point of 1-2 μm .

Characterization of HA-MMSN-1F12

Briefly, 1 mg/mL HA-MMSN and HA-MMSN-1F12 were prepared. Dynamic light scattering (DLS; photon correlation spectroscopy) and the Zetasizer Nano-ZS90 system (Malvern Instruments, Worcestershire, UK) were used to measure the size distribution and polydispersity index (PDI) of the nanoparticles.

Immunoprecipitation and Western blotting

Frozen tissues were homogenized in liquid nitrogen and extracted with tris-buffered saline (TBS, 20 mmol/L tris and 137 mmol/L NaCl, pH 7.6) solution as previously described [55, 59]. The homogenized supernatant was centrifuged at 10,000 \times g for 30 min at 4 $^{\circ}\text{C}$ to obtain TBS-soluble protein. The supernatant was aliquoted and stored at -80 $^{\circ}\text{C}$ before analysis. According to the manufacturer's guidance, brain homogenate or blood was incubated with 40 $\mu\text{g}/\text{mL}$ 1F12-conjugated protein A/G magnetic beads for 30 min at room temperature. Immunoprecipitated proteins were eluted with 0.1 M glycine (pH 3.0) and immediately neutralized to pH 7.4 with neutralization buffer (1 M Tris-HCl, pH 8.5). After boiling for 10 min, the denatured samples in the loading buffer (Boster Biotech, USA) were loaded on a 12% tris-tricine SDS-polyacrylamide gel electrophoresis (SDS-PAGE). Proteins were transferred to polyvinylidene fluoride (PVDF) membranes at 160 mA, 4 $^{\circ}\text{C}$ for 1.5 h, blocked with 5% skimmed milk in PBS-T, and then incubated with primary antibody 1F12 (1: 1,000, 5% skimmed milk) for 2 h at 37 $^{\circ}\text{C}$. Membranes were washed in PBS-T followed by 1 h incubation with a second antibody HRP-conjugated goat anti-mouse IgG (H+L) (1:4,000, PBS-T). The signal was detected with the ECL substrate (Vazyme, China) on a Tanon 5200 Multi (Shanghai, China).

Serum protein adsorption of HA-MMSN-1F12

To test whether HA-MMSN-1F12 has adsorption to serum protein, 15% fetal calf serum (FCS; 1 mg/mL) was incubated with HA-MMSN-1F12 at 37 $^{\circ}\text{C}$ for 24 h. Particles were isolated by centrifugation and washed twice with PBS. The particles were then dispersed in SDS buffer solution (10 mg/mL), mixed with Laemmli buffer after sonication for 30 min, and treated at 95 $^{\circ}\text{C}$ for 10 min before SDS-PAGE.

Sandwich enzyme-linked immunosorbent assay (ELISA)

Wells of a 96-well EIA/RIA plate were coated with 1 $\mu\text{g}/\text{well}$ of 1F12 and diluted in citrate-buffered saline (CBS) overnight at 4 $^{\circ}\text{C}$. All wells were blocked with 5% skimmed milk in PBS-T buffer for 2 h at 37 $^{\circ}\text{C}$. Next, standard series of $\text{A}\beta_{40}\text{Ms}$, $\text{A}\beta_{42}\text{Ms}$, $\text{A}\beta_{42}\text{ArcMs}$, $\text{A}\beta_{42}\text{Os}$, $\text{A}\beta_{42}\text{ArcOs}$, blood, and organ lysates were added to the wells in triplicate and incubated at 37 $^{\circ}\text{C}$ for 2 h. After washing 5 times with PBS-T, the wells were incubated with 1F12-HRP (1:500) at 37 $^{\circ}\text{C}$ for 1 h, followed by adding 100 μL of soluble TMB substrate solution at 37 $^{\circ}\text{C}$ for 15 min to reveal the immunoreactivity. Finally, plates were analyzed at 450 nm using an Epoch Microplate Spectrophotometer (Bio Tek, USA).

Indirect ELISA for detecting the specificity of HA-MMSN-1F12

Wells of a 96-well plate (Corning Inc, USA) were coated with 0.5 $\mu\text{g}/\text{well}$ of $\text{A}\beta_{40}\text{Ms}$, $\text{A}\beta_{42}\text{Ms}$, $\text{A}\beta_{42}\text{ArcMs}$, $\text{A}\beta_{42}\text{Os}$, and $\text{A}\beta_{42}\text{ArcOs}$ in citrate-buffered saline (CBS) overnight at 4 $^{\circ}\text{C}$. Wells coated with PBS were used as negative controls. All wells were blocked with 5% skim milk dissolved in PBS-T (PBS containing 0.1% Tween-20) buffer for 2 h at 37 $^{\circ}\text{C}$. Next, standard series of HA-MMSN, 1F12, and HA-MMSN-1F12 were added to the wells for 2 h incubation at 37 $^{\circ}\text{C}$, followed by the addition of a second antibody HRP-conjugated goat anti-mouse IgG (H+L) (1: 4,000, PBS-T) for 1 h incubation at 37 $^{\circ}\text{C}$. After 5 washes with PBS-T, 100 μL of soluble 3, 3', 5, 5'-tetramethylbenzidine (TMB) substrate solution (Tiangen Biotech, China) was added for visualization of immunoreactivity. Finally, the plate was analyzed at 450 nm with an Epoch Microplate Spectrophotometer (Bio Tek, USA).

Indirect ELISA for detecting the binding affinity of HA-MMSN-1F12

Wells of a 96-well plate were coated with 0.5 $\mu\text{g}/\text{well}$ of $\text{A}\beta_{40}\text{Ms}$, $\text{A}\beta_{42}\text{Ms}$, $\text{A}\beta_{42}\text{ArcMs}$, $\text{A}\beta_{42}\text{Os}$, and $\text{A}\beta_{42}\text{ArcOs}$, and blocked with 5% skimmed milk. Serial dilutions of 1F12, HA-MMSN, and HA-MMSN-1F12 from 1.0×10^{-5} mg/mL to 2.5×10^{-3} mg/mL were added to each well for 2 h incubation at 37 $^{\circ}\text{C}$. After incubation with 1F12-HRP (1:500) at 37 $^{\circ}\text{C}$ for 1 h, TMB substrate solution was added to visualize the immunoreactivity.

Construction of *in vitro* $\text{A}\beta_{42}$ aggregate degradation system

To evaluate the ability of HA-MMSN-1F12 to depolymerize insoluble $\text{A}\beta_{42}$ plaques, an *in vitro* degradation system of $\text{A}\beta_{42}$ aggregates was

constructed based on the transwell system. In this system, the upper and lower chambers are separated by a 5 kDa dialysis membrane. 500 μ L of 50 μ M A β ₄₂ aggregates in the upper chamber were incubated with 1 μ M HA-MMSN-1F12 or HA-MMSN-IgG in the lower chamber at 37 °C and the HA-MMSN-1F12 or HA-MMSN-IgG solution in the lower chamber was changed every 3 h. Then before incubation and 1, 3, 6, 9, 12, 15, and 18 h after incubation, 50 μ L of the upper chamber solution was taken for ThT fluorescence detection and sandwich ELISA to quantitatively analyze the content of A β ₄₂ aggregate in the upper chamber. TEM was used to detect the morphological changes of A β ₄₂ aggregate degraded into monomers in the upper chamber solution.

ThT fluorescence assay

The A β ₄₂ aggregate solution obtained from the above A β ₄₂ aggregate degradation assay was added to 100 μ L of 15 μ M ThT solution, respectively, and incubated in the dark for 15 min. Then, the fluorescence signal was recorded at an emission wavelength of 490 nm (excitation at 440 nm) by using a multiscan FC microplate photometer (Thermos, USA). All fluorescence experiments were repeated three times and averaged together with the standard deviation.

A β ₄₂ aggregate self-assembly inhibition assay

To evaluate the inhibitory effect of HA-MMSN-1F12 on A β ₄₂ aggregate assembly multimerization, 1 mL of 50 μ M A β ₄₂ monomer solution was incubated with 1 μ M HA-MMSN-1F12 at 37 °C on a shaker for 0, 1, 3, 6, 9, 12, 15, and 18 h, respectively. 100 μ L of the mixed solution was taken at the above different time points for ThT fluorescence detection.

Construction of the *in vitro* BBB model

To explore whether HA-MMSN-1F12 can cross the BBB and enter neuronal cells, a Transwell model was constructed to simulate the BBB. An *in vitro* BBB model was constructed based on human umbilical vein endothelial cells (HUVECs) for 7 days, and SY5Y cells were inoculated in Transwell lower chambers for 48 h, 1 μ M Cy3-labeled 1F12, HA-MMSN-1F12, HA-MMSN, and MMSN was added to the upper chambers at 37 °C. At 24 h, SY5Y cells were observed for confocal imaging.

Animals

All procedures involving animal studies have been reviewed and approved by the Institutional Animal Care and Use Committee of Huazhong University of Science and Technology. APPSwe/PS1dE9 (APP/PS1) transgenic mice were purchased from Beijing Huaifukang Biotechnology Co., Ltd. In

this study, APP/PS1 aged 6-10 months was used. All mice were housed in groups (5 mice per cage) under standard specific pathogen-free (SPF) conditions (12 h light/dark cycle, standard temperature 24 °C, humidity 50-60%, and pathogen-free).

In vitro fluorescence imaging and biodistribution of HA-MMSN-1F12

To evaluate the biodistribution of HA-MMSN-1F12, male APP/PS1 mice were divided into 5 groups of eight mice each. Animals were sacrificed at 6 h after intravenous injection of Cy5-labeled MMSN, HA-MMSN, 1F12, and HA-MMSN-1F12. An equal volume of PBS administered intravenously was used as a control. Mice were anesthetized with 0.4 mL Avertin (25 mg/mL) and perfused with 1 M PBS for 30 min. Major organs (brain and intestine) were collected, washed with PBS, weighed, and imaged on a black plate.

The total uptake of Cy5-labeled HA-MMSN-1F12 or other probes in major organs was determined by previously described quantitative methods [60, 61]. Here, 50 mg of each organ or blood was extracted by ultra-low temperature grinding, dissolved in 500 μ L of 3% (v/v) methanol, and centrifuged at 5,000 g for 10 min at 4 °C to remove debris. Then, 100 μ L of supernatant was transferred to a 96-well plate. The plate was analyzed at 647 nm with an Epoch Microplate Spectrophotometer (Bio Tek, USA). Standard curves for quantifying total 1F12 and HA-MMSN in organs were $y = 0.007x + 0.044$ ($R^2 = 0.9992$) and $y = 1.0363x + 0.0428$ ($R^2 = 0.9994$), respectively, x stands for 1F12 or HA-MMSN concentration, and y stands for fluorescence (Cy5) absorbance value. Under these conditions, the equation for %ID/g is $[(C_{\text{organ}} \times V_{\text{organ}}) / g_{\text{organ}}] / \text{ID/g} \times 100$, V_{organ} (mL) represents the tissue grind extraction volume of the region of interest, C_{organ} (mg/mL) represents the concentration of 1F12 or HA-MMSN in V_{organ} calculated according to the above standard curve, g_{organ} (g) represents the tissue weight of the region of interest, ID/g represents injected dose (4 mg/kg) in mice.

Immunofluorescence assays of slices

APP/PS1 mice were anesthetized with 0.4 mL Avertin (25 mg/mL) and perfused transcardially with 4% paraformaldehyde (PFA) for 30 min. The brain tissues were immersed in 4% PFA and stored in 30% sucrose in PBS. Tissues were sliced to a thickness of 25 μ m using a frozen Leica CM3050S microtome and mounted on an adhesion microscope slide (Jiangsu, China). Each tissue section was washed 3 times with 1 M PBS for 10 min and then washed with 0.2% Triton X-100 (Macklin, China) at room temperature for 20

min. The sections were blocked with 3% BSA for 2 h at room temperature and incubated with Cy5-labeled HA-MMSN-1F12, 1F12, or HA-MMSN-IgG overnight at 4 °C. Finally, all slices were washed with 1 M PBS and stained with ThioS. The Zeiss LSM710 microscope was used to image slices with Cy5, Alexa Fluor 488, and DAPI filters.

Thioflavin S counterstain

A β was counterstained with ThioS as previously described [62]. APP/PS1 tissues were sectioned 25 μ m thick and immunolabeled with Cy5-labeled HA-MMSN-1F12 or 1F12. Sections with or without Cy5 labeling were incubated with 0.002% ThioS solution in TBS (diluted from 0.02% ThioS stock solution in distilled water) for 30 min, then washed 3 times in 50% ethanol (v/v), with a final wash in 1 M PBS 3 times for 5 min each. Sections were mounted with 50% glycerol reagent (m/v) and images were acquired under fluorescence microscopy at 10x magnification and analyzed by Image J software.

Flow cytometric analysis of KCs

Flow cytometric analysis of KCs was performed using previously described methods [63, 64]. The hepatic low-pressure portal vein was perfused with collagenase type IV solution and digested with collagenase type IV and DNase I at 37 °C. The mixture was filtered using a 70 μ m cell strainer (BD, USA), and tissue debris was removed by centrifugation at 400 \times g for 2 min to obtain hepatocytes. The cell pellets were resuspended in 3 mL of RPMI1640 medium, and 5 mL of 70% Percoll and 7 mL of 30% Percoll were added to the cell solution along the wall of the 15 mL tube. KCs were obtained after centrifugation at 500 \times g for 20 min to remove the intermediate layer.

KCs (1×10^5 /well) were incubated with Alexa Fluor 488-labeled 1 μ M HA-MMSN-1F12, HA-MMSN, MMSN, and 1F12 for 2 h at 37 °C in a humidified incubator with 5% CO₂ to analyze the phagocytosis of nanoparticles by KCs. Then, KCs were washed with PBS and stained with AlexaFluor 647-labeled anti-mouse F4/80 (1:400, Abcam, England). After 1 h incubation, KCs were washed three times with PBS to remove excess AlexaFluor 647-labeled anti-mouse F4/80. Finally, the fluorescence intensity of KCs was examined using a CytoFLEX flow cytometer (Beckman Coulter, USA). Confocal images of KCs were acquired using a Zeiss LSM710 confocal imaging system (Oberkochen, Germany). Data were analyzed using FlowJo software (FlowJo, Ashland, OR, USA) and ImageJ software, respectively.

Evaluation of the effect of HA-MMSN-1F12 targeting A β in the brain of APP/PS1 mice

To assess the effect of HA-MMSN-1F12 targeting

A β in the brains of APP/PS1 mice, ten-month-old male APP/PS1 mice (n = 3) were intravenously injected with Cy5-labeled HA-MMSN-1F12 at a dose of 12 mg/kg. At 6 h post-injection, mice were anesthetized with 0.4 mL of Avertin (25 mg/mL) and perfused with 1 M PBS for 30 min. Next, brains were collected, fixed in 4% PFA solution, and completely dehydrated in 30% sucrose solution. Brain tissues were sliced to a thickness of 25 μ m using a freezing Leica CM3050S microtome. Finally, all slices were washed with 1 M PBS and stained with ThioS.

In vivo brain MRI of APP/PS1 mice

After injection of 100 μ g HA-MMSN-1F12 into APP/PS1 mice, APP/PS1 mouse brains were performed magnetic resonance imaging (MRI) at 0, 3, and 9 h using a Bruker Biospec system (BioSpec 70/20USR, Billerica, MA) at 7.0 T (proton resonance frequency 300M Hz, aperture 20 cm). During the scan, the mice were anesthetized by inhaling 1-1.5% isoflurane in 30%/70% O₂/N₂. T2* weighting parameters are as follows: repetition time (TR) = 2500 ms, echo time (ET) = 29 ms, rarity factor = 8, field of view (FOV) = 1.80 cm \times 1.80 cm, in-plane resolution = 0.07 cm, single layer thickness = 0.6 cm, a total of 25 slices. T2-weighted images provide more localization of HA-MMSN-1F12 because iron causes local changes in susceptibility to which T2-weighted images are sensitive.

Immunohistochemistry (IHC)

To detect the expression changes of CD86 in the brain after treatment, the brain tissue of the treated mice was sliced into a thickness of 25 μ m. Antigen retrieval buffer at pH 9.0 was used for each brain section at 98 °C for 20 min. Sections were blocked with 3% BSA for 2 h at room temperature and incubated with anti-CD86 primary antibody overnight at 4 °C. All sections were then washed three times with TBS buffer and incubated with alkaline phosphatase (AP) polymeric anti-mouse IgG for 1 h at 37 °C. Finally, the sections were observed under light microscopy (Nikon, Japan).

Quantitative assays of inflammatory factors

The BD cytometric bead array (CBA) Mouse Th1/Th2/Th17 cytokine kit was used to quantitatively estimate the expression of inflammatory factors in the brain. The procedure was performed according to the protocol provided by the manufacturer (Catalog No.560485, BD).

Transcriptome analysis

Mouse brain tissue was collected and stored at -80 °C for sequencing. Raw transcriptome data were generated by Illumina's high-throughput sequencing

platform. The “Limma” package was used for differentially expressed genes (DEGs) analysis. An empirical Bayesian approach was used to estimate the fold change between cluster 1 and cluster 2, which was determined by a consensus clustering method using a modest t-test [65]. The Benjamini-Hochberg correction was used to calculate the adjusted P-value for multiple tests. Genes with an absolute log₂ fold change greater than 1.5 were identified as DEGs between the two clusters. DEGs was used as input for pathway analysis. $|FC| > 2$ and $\text{adj.p.val} < 0.05$ were used as cut-off thresholds. Gene Ontology (GO) and Kyoto Encyclopedia of Genes and Genomes (KEGG) enrichment analyses were performed by the “cluster profile” R package.

Morris water maze assay

The morris water maze setup consists of a circular tube (diameter, 120 cm; height, 50 cm) and a platform (diameter, 10 cm) that sits 1 cm below the water surface. The standard water temperature was 20–22 °C, and each mouse was tested in 4 quadrants per day for 5 consecutive days. If the mouse finds an underwater platform within 60 s, let it stay on the platform for 30 s. If the mouse does not find an underwater platform within 60 s and stays on the underwater platform for 3 s, it is directed to the platform and stays on the platform for 30 s. On the sixth day, the underwater platform was dismantled. Each mouse was placed in the bathtub from the opposite position to the original quadrant and swim for 60 s.

In vitro biostability of HA-MMSN-1F12

In vitro biodegradation of HA-MMSN-1F12 was performed as previously described [58]. Briefly, 50 µg of HA-MMSN-1F12 was incubated in Krebs-Henseleit solution (D-glucose 2.0 g/L, magnesium sulfate 0.141 g/L, potassium phosphate monobasic 0.16 g/L, potassium chloride 0.35 g/L, sodium chloride 6.9 g/L, calcium chloride dihydrate 0.373 g/L, and sodium bicarbonate 2.1 g/L) at 37 °C for 12, 24, 48, 72, 96, and 144 h. TEM images of the sample were acquired at the indicated time points.

Blood biochemical analysis

To evaluate the side effects of HA-MMSN-1F12, 8-week-old male C57BL/6 mice were injected intravenously with 100 mg/kg of HA-MMSN-1F12 per mouse. PBS was used as a control. Blood samples were collected from mice at 24 h after intravenous injection of HA-MMSN-1F12 or PBS. Biochemical analysis was performed using an automated biochemical analyzer (Spotchem EZ SP-4430, Arkray Inc., Kyoto, Japan) and SPOTCHEM II reagent test strips. We performed metabolic measurements in

blood, including blood urea nitrogen (BUN), albumin (ALB), alkaline phosphatase (ALP), alanine aminotransferase (ALT), creatinine (CRE), and globulins (GLOB).

Histopathological analysis

Hearts, livers, spleens, kidneys, and lungs were extracted from mice on day 7 after intravenous injection of HA-MMSN-1F12 or PBS and fixed in 4% PFA solution overnight. Organs were embedded in paraffin, sectioned, and stained with hematoxylin and eosin (H&E). H&E sections were imaged on a Nikon Ni-E microscope (Nikon, Minato, Tokyo, Japan). All images were acquired using NIS-Elements software and further analyzed using ImageJ software.

Statistical analysis

Statistical analysis was performed using GraphPad Prism version 8.0. All values in the graphs are expressed as mean ± standard error of the mean (SEM) and are used to represent approximately normally distributed continuous variables. One-way or two-way analysis of variance (ANOVA) was used for multiple group comparisons. Statistical significance is indicated in the graph with * $p < 0.05$, ** $p < 0.01$, *** $p < 0.001$, **** $p < 0.0001$, and n.s. (indicating no significance).

Abbreviations

Aβ: amyloid-β; AD: Alzheimer's disease; HA: hyaluronic acid; APP: amyloid precursor protein; BBB: blood-brain barrier; mAb: anti-Aβ monoclonal antibody; TfR: Transferrin receptor; LRP1: low-density lipoprotein receptor-related protein-1; FT-IR: Fourier transform infrared; SR: saturation recovery; MSN: Mesoporous silica nanoparticle; MMSN: magnetic mesoporous silica nanosphere; KCs: Kuffer cells; IHC: Immunohistochemistry; MRI: magnetic resonance imaging; HRP: Poly-Horseradish Peroxidase; DMSO: Dimethyl sulfoxide; BSA: bovine serum albumin; NHS: N-hydroxysuccinimide; DAPI: 4',6-diamidino-2-phenylindole; OA: Oleic acid; CTAB: N-cetyltrimethylammonium bromide; TEOS: Tetraethyl orthosilicate; Aβ₄₀Ms: Aβ₄₀ monomers; Aβ₄₂Ms: Aβ₄₂ monomers; Aβ₄₂ArcMs: Aβ₄₂Arc monomers; Aβ₄₂ArcO: Aβ₄₂Arc oligomer; PBS: phosphate-buffered saline; CBS: citrate-buffered saline; TMB: 3, 3', 5, 5'-tetramethylbenzidine; TBS: tris-buffered saline; GO: Gene ontology; KEGG: Kyoto encyclopedia of genes and genomes; SDS-PAGE: sulfate-polyacrylamide gel electrophoresis; ThioS: Thioflavin S; DEGs: differentially expressed genes; mt-Atp6: membrane subunit 6; H&E: hematoxylin and eosin; CBA: cytometric bead array; AP: alkaline phosphatase; ET: echo time; FOV: field of view; PFA:

paraformaldehyde; SPF: specific pathogen-free; FCS: fetal calf serum; HUVECs: human umbilical vein endothelial cells; PDI: polydispersity index; CSF: cerebrospinal fluid; PKC- α : protein kinase C- α ; Th: tyrosine hydroxylase; ALB: albumin; ALP: alkaline phosphatase; ALT: alanine aminotransferase; BUN: blood urea nitrogen; CRE: creatinine; GLOB: globulins.

Supplementary Material

Supplementary figures.

<https://www.thno.org/v12p6646s1.pdf>

Acknowledgments

This study was financially supported by grants from the Major Research Plan of the National Natural Science Foundation of China (Grant No. 91749209) and the National Natural Science Foundation of China (Grant No. 81971025). We also thank the Optical Bioimaging Core Facility and the Center for Nanoscale Characterization & Devices (CNCD) of WNLO-HUST for support with data acquisition, the Analytical and Testing Center of HUST for performing spectral measurements, and the Research Core Facilities for Life Science (HUST) for using cryo-transmission electron microscopy.

Author contributions

L.H. and L.Q. provided conceptualization, writing guidance, and manuscript revision. L.N. completed all experiments and contributed to writing the first draft. Y.C. assisted data analysis. L.X. and H.S. participated in experiments. All authors reviewed and approved the final manuscript.

Competing Interests

The authors have declared that no competing interest exists.

References

- Zhang L, Liang X, Zhang Z, Luo H. Cerebrospinal fluid and blood biomarkers in the diagnostic assays of Alzheimer's disease. *J Innov Opt Health Sci.* 2022; 15: 2230001.
- Xiang Y, Bu XL, Liu YH, Zhu C, Shen LL, Jiao SS, et al. Physiological amyloid-beta clearance in the periphery and its therapeutic potential for Alzheimer's disease. *Acta Neuropathol.* 2015; 130: 487-99.
- Salloway S, Honigberg LA, Cho W, Ward M, Friesenhahn M, Brunstein F, et al. Amyloid positron emission tomography and cerebrospinal fluid results from a crenesumab anti-amyloid-beta antibody double-blind, placebo-controlled, randomized phase II study in mild-to-moderate Alzheimer's disease (BLAZE). *Alzheimers Res Ther.* 2018; 10: 96.
- Bard F, Cannon C, Barbour R, Burke RL, Games D, Grajeda H, et al. Peripherally administered antibodies against amyloid beta-peptide enter the central nervous system and reduce pathology in a mouse model of Alzheimer disease. *Nat Med.* 2000; 6: 916-9.
- Fisher DG, Price RJ. Recent Advances in the Use of Focused Ultrasound for Magnetic Resonance Image-Guided Therapeutic Nanoparticle Delivery to the Central Nervous System. *Front Pharmacol.* 2019; 10: 1348.
- Wang Z, Xiong G, Tsang WC, Schatzlein AG, Uchegbu IF. Nose-to-Brain Delivery. *J Pharmacol Exp Ther.* 2019; 370: 593-601.
- Terstappen GC, Meyer AH, Bell RD, Zhang W. Strategies for delivering therapeutics across the blood-brain barrier. *Nat Rev Drug Discov.* 2021; 20: 362-83.

- Boado RJ, Zhou QH, Lu JZ, Hui EK, Pardridge WM. Pharmacokinetics and brain uptake of a genetically engineered bifunctional fusion antibody targeting the mouse transferrin receptor. *Mol Pharm.* 2010; 7: 237-44.
- Pardridge WM, Kang YS, Buciaci JL, Yang J. Human insulin receptor monoclonal antibody undergoes high affinity binding to human brain capillaries *in vitro* and rapid transcytosis through the blood-brain barrier *in vivo* in the primate. *Pharm Res.* 1995; 12: 807-16.
- Hultqvist G, Syvanen S, Fang XT, Lannfelt L, Sehlin D. Bivalent Brain Shuttle Increases Antibody Uptake by Monovalent Binding to the Transferrin Receptor. *Theranostics.* 2017; 7: 308-18.
- Niewoehner J, Bohrmann B, Collin L, Urich E, Sade H, Maier P, et al. Increased brain penetration and potency of a therapeutic antibody using a monovalent molecular shuttle. *Neuron.* 2014; 81: 49-60.
- Boado RJ, Zhang Y, Zhang Y, Xia CF, Pardridge WM. Fusion antibody for Alzheimer's disease with bidirectional transport across the blood-brain barrier and abeta fibril disaggregation. *Bioconjug Chem.* 2007; 18: 447-55.
- Sehlin D, Fang XT, Cato L, Antoni G, Lannfelt L, Syvanen S. Antibody-based PET imaging of amyloid beta in mouse models of Alzheimer's disease. *Nat Commun.* 2016; 7: 10759.
- Guo Q, Zhu Q, Miao T, Tao J, Ju X, Sun Z, et al. LRP1-upregulated nanoparticles for efficiently conquering the blood-brain barrier and targetedly suppressing multifocal and infiltrative brain metastases. *J Control Release.* 2019; 303: 117-29.
- Yu YJ, Zhang Y, Kenrick M, Hoyte K, Luk W, Lu Y, et al. Boosting brain uptake of a therapeutic antibody by reducing its affinity for a transcytosis target. *Sci Transl Med.* 2011; 3: 84ra44.
- Syvanen S, Hultqvist G, Gustavsson T, Gumucio A, Laudon H, Soderberg L, et al. Efficient clearance of Abeta protofibrils in AbetaPP-transgenic mice treated with a brain-penetrating bifunctional antibody. *Alzheimers Res Ther.* 2018; 10: 49.
- Bien-Ly N, Yu YJ, Bumbaca D, Elstrodt J, Boswell CA, Zhang Y, et al. Transferrin receptor (TfR) trafficking determines brain uptake of TfR antibody affinity variants. *J Exp Med.* 2014; 211: 233-44.
- Villasenor R, Schilling M, Sundaresan J, Lutz Y, Collin L. Sorting Tubules Regulate Blood-Brain Barrier Transcytosis. *Cell Rep.* 2017; 21: 3256-70.
- Ventorp F, Barzilay R, Erhardt S, Samuelsson M, Traskman-Bendz L, Janelidze S, et al. The CD44 ligand hyaluronic acid is elevated in the cerebrospinal fluid of suicide attempters and is associated with increased blood-brain barrier permeability. *J Affect Disord.* 2016; 193: 349-54.
- Kesharwani P, Chadar R, Sheikh A, Rizq WY, Safhi AY. CD44-Targeted Nanocarrier for Cancer Therapy. *Front Pharmacol.* 2021; 12: 800481.
- Nicolas J, Mura S, Brambilla D, Mackiewicz N, Couvreur P. Design, functionalization strategies and biomedical applications of targeted biodegradable/biocompatible polymer-based nanocarriers for drug delivery. *Chem Soc Rev.* 2013; 42: 1147-235.
- Ordóñez-Gutiérrez L, Re F, Bereczki E, Joja E, Gregori M, Andersen AJ, et al. Repeated intraperitoneal injections of liposomes containing phosphatidic acid and cardiolipin reduce amyloid-beta levels in APP/PS1 transgenic mice. *Nanomedicine.* 2015; 11: 421-30.
- Carradori D, Balducci C, Re F, Brambilla D, Le Droumaguet B, Flores O, et al. Antibody-functionalized polymer nanoparticle leading to memory recovery in Alzheimer's disease-like transgenic mouse model. *Nanomedicine.* 2018; 14: 609-18.
- Brambilla D, Verpillot R, Le Droumaguet B, Nicolas J, Taverna M, Kona J, et al. PEGylated nanoparticles bind to and alter amyloid-beta peptide conformation: toward engineering of functional nanomedicines for Alzheimer's disease. *ACS Nano.* 2012; 6: 5897-908.
- Kim D, Kwon HJ, Hyeon T. Magnetite/Ceria Nanoparticle Assemblies for Extracorporeal Cleansing of Amyloid-beta in Alzheimer's Disease. *Adv Mater.* 2019; 31: e1807965.
- Schafer KH, Christmann A, Gries M. Can we trust the gut? The role of the intestine in neurodegeneration. *J Physiol.* 2020; 598: 4141-2.
- Maarouf CL, Walker JE, Sue LL, Dugger BN, Beach TG, Serrano GE. Impaired hepatic amyloid-beta degradation in Alzheimer's disease. *PLoS One.* 2018; 13: e0203659.
- Lam V, Takechi R, Hackett MJ, Francis R, Bynevelt M, Celliers LM, et al. Synthesis of human amyloid restricted to liver results in an Alzheimer disease-like neurodegenerative phenotype. *PLoS Biol.* 2021; 19: e3001358.
- Colino CI, Lanoa JM, Gutierrez-Millan C. Targeting of Hepatic Macrophages by Therapeutic Nanoparticles. *Front Immunol.* 2020; 11: 218.
- Chan WT, Liu CC, Chiang Chiaui JS, Tsai ST, Liang CK, Cheng ML, et al. *In vivo* toxicologic study of larger silica nanoparticles in mice. *Int J Nanomedicine.* 2017; 12: 3421-32.
- Sohaebuddin SK, Thevenot PT, Baker D, Eaton JW, Tang L. Nanomaterial cytotoxicity is composition, size, and cell type dependent. *Part Fibre Toxicol.* 2010; 7: 22.
- Zhang L, Yang C, Li Y, Niu S, Liang X, Zhang Z, et al. Dynamic changes in the levels of amyloid- β 42 species in the brain and periphery of APP/PS1 mice and their significance for Alzheimer's disease. *Front Mol Neurosci.* 2021; 14: 723317.
- Li PZ, Li JZ, Li M, Gong JP, He K. An efficient method to isolate and culture mouse Kupffer cells. *Immunol Lett.* 2014; 158: 52-6.
- Park JS, Kam TI, Lee S, Park H, Oh Y, Kwon SH, et al. Blocking microglial activation of reactive astrocytes is neuroprotective in models of Alzheimer's disease. *Acta Neuropathol Commun.* 2021; 9: 78.

35. Navarro V, Sanchez-Mejias E, Jimenez S, Munoz-Castro C, Sanchez-Varo R, Davila JC, et al. Microglia in Alzheimer's Disease: Activated, Dysfunctional or Degenerative. *Front Aging Neurosci.* 2018; 10: 140.
36. Harry GJ, Kraft AD. Microglia in the developing brain: a potential target with lifetime effects. *Neurotoxicology.* 2012; 33: 191-206.
37. Edler MK, Sherwood CC, Meindl RS, Munger EL, Hopkins WD, Ely JJ, et al. Microglia changes associated to Alzheimer's disease pathology in aged chimpanzees. *J Comp Neurol.* 2018; 526: 2921-36.
38. Wang Z, Zhang R, Yan X, Fan K. Structure and activity of nanozymes: Inspirations for de novo design of nanozymes. *Materials Today.* 2020; 41: 81-119.
39. Xu C, Nam J, Hong H, Xu Y, Moon JJ. Positron Emission Tomography-Guided Photodynamic Therapy with Biodegradable Mesoporous Silica Nanoparticles for Personalized Cancer Immunotherapy. *ACS Nano.* 2019; 13: 12148-61.
40. Jong A, Wu CH, Prasadarao NV, Kwon-Chung KJ, Chang YC, Ouyang Y, et al. Invasion of *Cryptococcus neoformans* into human brain microvascular endothelial cells requires protein kinase C- α activation. *Cell Microbiol.* 2008; 10: 1854-65.
41. Long M, Huang S-H, Wu C-H, Shackelford GM, Jong A. Lipid raft/caveolae signaling is required for *Cryptococcus neoformans* invasion into human brain microvascular endothelial cells. *J Biomed Sci.* 2012; 19: 1-14.
42. Santiago-Tirado FH, Onken MD, Cooper JA, Klein RS, Doering TL. Trojan Horse Transit Contributes to Blood-Brain Barrier Crossing of a Eukaryotic Pathogen. *mBio.* 2017; 8.
43. Tavares AJ, Poon W, Zhang YN, Dai Q, Besla R, Ding D, et al. Effect of removing Kupffer cells on nanoparticle tumor delivery. *Proc Natl Acad Sci U S A.* 2017; 114: E10871-E80.
44. Poon W, Zhang YN, Ouyang B, Kingston BR, Wu JLY, Wilhelm S, et al. Elimination Pathways of Nanoparticles. *ACS Nano.* 2019; 13: 5785-98.
45. Yu W, Liu R, Zhou Y, Gao H. Size-Tunable Strategies for a Tumor Targeted Drug Delivery System. *ACS Cent Sci.* 2020; 6: 100-16.
46. Hoshi T, Nakahara T, Fukawa T, Takabayashi K, Gunji A. [The structural analysis of inpatient medical cost of the aged in 81 secondary medical areas of 12 Prefectures in Japan]. *Nihon Kosshu Eisei Zasshi.* 1995; 42: 869-77.
47. Zhou Y, Dai Z. New Strategies in the Design of Nanomedicines to Oppose Uptake by the Mononuclear Phagocyte System and Enhance Cancer Therapeutic Efficacy. *Chem Asian J.* 2018; 13: 3333-40.
48. Perkins KA, Grobe JE, Stiller RL, Fonte C, Goettler JE. Nasal spray nicotine replacement suppresses cigarette smoking desire and behavior. *Clin Pharmacol Ther.* 1992; 52: 627-34.
49. Demattos RB, Lu J, Tang Y, Racke MM, Delong CA, Tzaferis JA, et al. A plaque-specific antibody clears existing beta-amyloid plaques in Alzheimer's disease mice. *Neuron.* 2012; 76: 908-20.
50. Hu S, Yang C, Luo H. Current trends in blood biomarker detection and imaging for Alzheimer's disease. *Biosens Bioelectron.* 2022; 210: 114278.
51. Zhang L, Du X, Su Y, Niu S, Li Y, Liang X, et al. Quantitative assessment of AD markers using naked eyes: point-of-care testing with paper-based lateral flow immunoassay. *J Nanobiotechnology.* 2021; 19: 366.
52. Salvatore C, Cerasa A, Castiglioni I. MRI Characterizes the Progressive Course of AD and Predicts Conversion to Alzheimer's Dementia 24 Months Before Probable Diagnosis. *Front Aging Neurosci.* 2018; 10: 135.
53. Kas A, Migliaccio R, Tavittian B. A future for PET imaging in Alzheimer's disease. *Eur J Nucl Med Mol Imaging.* 2020; 47: 231-4.
54. Pascoal TA, Benedet AL, Ashton NJ, Kang MS, Theriault J, Chamoun M, et al. Microglial activation and tau propagate jointly across Braak stages. *Nat Med.* 2021; 27: 1592-9.
55. Jin WS, Shen LL, Bu XL, Zhang WW, Chen SH, Huang ZL, et al. Peritoneal dialysis reduces amyloid-beta plasma levels in humans and attenuates Alzheimer-associated phenotypes in an APP/PS1 mouse model. *Acta Neuropathol.* 2017; 134: 207-20.
56. Yang K, Peng H, Wen Y, Li N. Re-examination of characteristic FTIR spectrum of secondary layer in bilayer oleic acid-coated Fe₃O₄ nanoparticles. *Applied Surface Science.* 2010; 256: 3093-7.
57. Wu Q, Li Q, Zhang X, Ntim M, Wu X, Li M, et al. Treatment with Bifidobacteria can suppress A β accumulation and neuroinflammation in APP/PS1 mice. *PeerJ.* 2020; 8: e10262.
58. Hou G, Qian J, Xu W, Sun T, Wang Y, Wang J, et al. A novel pH-sensitive targeting polysaccharide-gold nanorod conjugate for combined photothermal-chemotherapy of breast cancer. *Carbohydr Polym.* 2019; 212: 334-44.
59. Englund H, Sehlin D, Johansson AS, Nilsson LN, Gellerfors P, Paulie S, et al. Sensitive ELISA detection of amyloid-beta protofibrils in biological samples. *J Neurochem.* 2007; 103: 334-45.
60. Zheng X, Shao X, Zhang C, Tan Y, Liu Q, Wan X, et al. Intranasal H102 Peptide-Loaded Liposomes for Brain Delivery to Treat Alzheimer's Disease. *Pharm Res.* 2015; 32: 3837-49.
61. Ahmad E, Feng Y, Qi J, Fan W, Ma Y, He H, et al. Evidence of nose-to-brain delivery of nanoemulsions: cargoes but not vehicles. *Nanoscale.* 2017; 9: 1174-83.
62. Viola KL, Sbarboro J, Sureka R, De M, Bicca MA, Wang J, et al. Towards non-invasive diagnostic imaging of early-stage Alzheimer's disease. *Nat Nanotechnol.* 2015; 10: 91-8.
63. Lin Q, Deng D, Song X, Dai B, Yang X, Luo Q, et al. Self-Assembled "Off/On" Nanopomegranate for *In Vivo* Photoacoustic and Fluorescence Imaging: Strategic Arrangement of Kupffer Cells in Mouse Hepatic Lobules. *ACS Nano.* 2019; 13: 1526-37.
64. Heymann F, Peusquens J, Ludwig-Portugall I, Kohlhepp M, Ergen C, Niemiets P, et al. Liver inflammation abrogates immunological tolerance induced by Kupffer cells. *Hepatology.* 2015; 62: 279-91.
65. Ritchie ME, Phipson B, Wu D, Hu Y, Law CW, Shi W, et al. limma powers differential expression analyses for RNA-sequencing and microarray studies. *Nucleic Acids Res.* 2015; 43: e47.